Martínez Casas, J.; Di Gialleonardo, E.; Bruni, S.; Baeza González, LM. (2014). A comprehensive model of the railway wheelset-track interaction in curves. Journal of Sound and Vibration. 333(18):4152-4169. doi:10.1016/j.jsv.2014.03.032.

A comprehensive model of the railway wheelset-track interaction in curves

Authors: José Martínez-Casas[1], Egidio Di Gialleonardo[2], Stefano Bruni[2], Luis Baeza[1*]

Affiliation:

[1]Centro de Investigación de Tecnología de Vehículos, Universitat Politècnica de València, Camino de Vera s/n, 46022 Valencia, Spain

[2]Dipartimento di Meccanica, Politecnico di Milano, Via La Masa 1, 20156 Milano, Italy

* Corresponding author

E-mail corresponding author: *baeza@mcm.upv.es*

Short title: Railway wheelset-track interaction in curves

Address for correspondence:

Luis Baeza
Departamento de Ingeniería Mecánica y de Materiales.
Universidad Politécnica de Valencia.
Camino de Vera s.n.,
46022 Valencia.
Spain.
Tl: +34 963877621
Fax: +34 963877629
e-mail: *baeza@mcm.upv.es*

Abstract

Train-track interaction has been extensively studied in the last 40 years at least, leading to modelling approaches that can deal satisfactorily with many dynamic problems arising at the wheel/rail interface. However, the available models are usually not considering specifically the running dynamics of the vehicle in a curve, whereas a number of train-track interaction phenomena are specific to curve negotiation.

The aim of this paper is to define a model for a flexible wheelset running on a flexible curved track. The main novelty of this work is to combine a trajectory coordinate set with Eulerian modal coordinates; the former permits to consider curved tracks, and the latter models the small relative displacements between the trajectory frame and the solid. In order to reduce the computational complexity of the problem, one single flexible wheelset is considered instead of one complete bogie, and suitable forces are prescribed at the primary suspension seats so that the mean values of the creepages and contact forces are consistent with the low frequency curving dynamics of the complete vehicle.

The wheelset model is coupled to a cyclic track model having constant curvature by means of a wheel/rail contact model which accounts for the actual geometry of the contacting profiles and for the non-linear relationship between creepages and creep forces.

The proposed model can be used to analyse a variety of dynamic problems for railway vehicles, including rail corrugation and wheel polygonalisation, squeal noise, numerical estimation of the wheelset service loads. In this paper, simulation results are presented for some selected running conditions to exemplify the application of the model to the study of realistic train-track interaction cases and to point out the importance of curve negotiation effects specifically addressed in the work.

Keywords

Flexible wheelset, flexible curved track, train-track interaction

1. INTRODUCTION

Train-track interaction consists of the coupled vibration of a railway vehicle or train set and of a flexible track, with coupling of the two sub-systems being provided by wheel-rail contact forces and excitation arising mainly from surface imperfections in the rails and wheels, such as rail roughness and wheel out-of-roundness. In some cases, large level of vibration and large dynamic fluctuations of the contact forces may take place, leading to unwanted phenomena such as high levels of noise and vibration [1], damage of the rolling surfaces in the form of corrugation [2] or rolling contact fatigue [3]. Furthermore, train-track interaction also leads to dynamic stresses in the track components and in the wheelsets, which need to be carefully considered in order to avoid failures due to metal fatigue.

For these reasons, a large effort has been spent over the last 40 years to define suitable models for studying train-track interaction. Early models were mostly based on the representation of the vehicle as a system formed by rigid bodies, possibly simplified to considering only the wheelset as a rigid mass resting on a Hertzian stiffness [4]. More recently, the need to widen the frequency range of analysis led to the incorporation of wheelset flexibility in the models, leading to a more realistic representation of wheel-rail interaction effects at higher frequencies. For the study of rail corrugation and wheel polygonalisation, generally a modal synthesis is introduced to reduce the size of the problem [5 – 7], whereas in case the frequency range of interest is up to 1kHz and above (such as for the study of rolling noise) a Finite Element model of the wheel or the wheelset is used without condensation [8, 9]. Only very recently, a further model refinement was introduced to consider the inertial effects due to wheelset rotation [10, 11].

It should be noted that many phenomena related with train-track interaction, particularly squeal noise, short pitch rail corrugation and the largest stresses generated in the wheels and axle are mostly occurring when the rail vehicle negotiates a curved track, calling for a proper consideration of the effects related with wheelset curving in train-track interaction models. When a rail vehicle runs through a curve, two mutually influencing phenomena take place at wheel rail contact: on one hand, contact parameters such as the contact point position, the normal and creep forces and the creepages are slowly evolving in response to curve negotiation; on the other hand, the same quantities are subject to faster changes due to high-frequency interaction of the flexible bodies in contact. On account of the non-linearity of the problem, the two effects cannot be superimposed and a more comprehensive approach needs to be deployed which, to the Authors' knowledge, has not been presented yet.

The aim of this paper is therefore to propose a mathematical model for the dynamics of a flexible wheelset running through a curve and interacting with a flexible railway track, considering in full the nonlinearities introduced by wheel-rail contact. In order to reduce the computational complexity of the problem, one single flexible wheelset is considered instead of one complete bogie, and forces are prescribed at the primary suspension seats, according to a procedure described in Section 2.2, so that the mean values of the creepages and contact forces are consistent with the low frequency curving dynamics of the complete vehicle.

A trajectory coordinates set is introduced that permits to describe the large motion of the wheelset along the curved track, and the small relative movements of the wheelset with respect to the trajectory frame are described by means of Eulerian modal coordinates introduced with respect to a set of modal shapes obtained from a finite element model of the wheelset. The wheelset model is coupled to a cyclic track model having constant curvature by means of a wheel/rail contact model which accounts for the actual geometry of the contacting profiles and for the nonlinear relationship between creepages and creep forces. In the track model, the rails are modelled as Timoshenko beam elements, this confines the range of validity for the complete wheelset-track model to 1.5 kHz, see Section 3. In order to avoid errors associated with modal truncation, the modes considered for the track and the wheelset are covering a frequency range wider than the range of validity of the track model, as detailed in Sections 2.1 and 3 of the paper.

Results for the proposed modelling approach are presented for a selected vehicle type and curving condition and for different excitation sources including short wavelength geometric imperfections in the rail profiles and singularities such as wheel flats. Results are also shown considering the wheelset running in tangent track, to point out the importance of curve negotiation effects specifically addressed in this work.

The paper is organised as follows: in Section 2 the equations of motion for the flexible wheelset in a curve are derived. In Section 3 the model of a cyclic curved flexible track is presented. In Section 4 the model of wheel-rail contact forces is introduced and the final equations of the train-track interaction problem are obtained. In Section 5 simulation results are presented for some selected running conditions and finally in Section 6 conclusive remark are provided.

2. THE FLEXIBLE WHEELSET MODEL IN CURVED TRACK

The study of vehicle-track interaction is carried out in this paper considering one single wheelset, given that in the frequency range of interest the dynamics of the sprung masses (bogie frame and car body) are effectively isolated from the motion of the un-sprung masses (wheelsets and axle

boxes) on account of the mechanical filter introduced by the suspensions. The effect of low frequency curving dynamics of the complete vehicle needs however to be included in the model, in order to obtain suitable mean values for the creepages and contact forces, which affect the coupled wheelset-track vibration also at higher frequency. This is accomplished by prescribing the forces applied by the primary suspension to the wheelset in the vertical plane and the yaw rotation of the bogie at the primary suspension, as explained in Section 2.2.

2.1. Equations of motion of the flexible wheelset

Fig. 1 shows the reference frames and position vectors used to describe the motion of the wheelset in a curve. In order to model the flexible wheelset travelling on curved track, two reference frames are considered. The first one is an inertial frame $\mathbf{X}_0\mathbf{Y}_0\mathbf{Z}_0$ which is fixed in an arbitrary point. The second is a trajectory coordinate frame $\mathbf{X}_T\mathbf{Y}_T\mathbf{Z}_T$ that follows the motion of the wheelset. The system $\mathbf{X}_T\mathbf{Y}_T\mathbf{Z}_T$ is centred in the undeformed configuration of the wheelset, with the $\mathbf{X}_T$-axis parallel to the forward speed, the $\mathbf{Y}_T$-axis parallel to wheelset axis and the $\mathbf{Z}_T$-axis pointing upwards. A vector referred to the fixed and trajectory frame is denoted by $\mathbf{a}_0$ and $\mathbf{a}$, respectively.

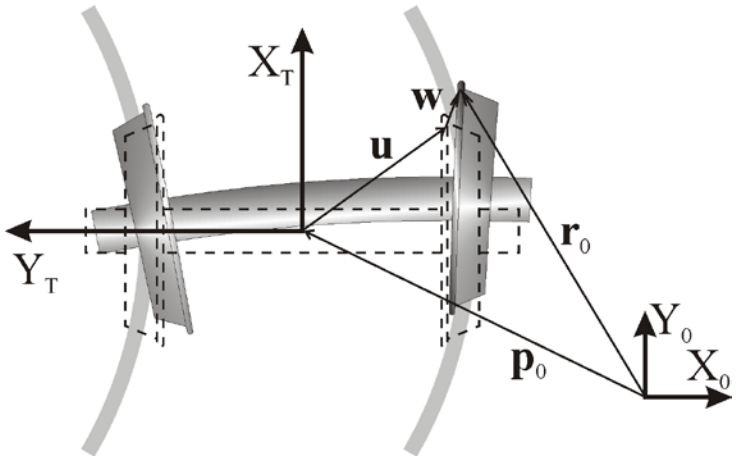

Figure 1: Reference frames and position vectors. The undeformed configuration of the wheelset is shown in dashed trace; a generic position of the flexible wheelset is sketched in solid colours.

The coordinates that are implemented in the wheelset model do not follow the material points of the solid which is the most common procedure in Mechanics, nonetheless they are associated with spatial points (Eulerian approach). The position vector $\mathbf{r}_0$ of a material particle which is in the spatial position $\mathbf{u}$ at instant t for the undeformed configuration, can be defined by means of the following formula:

$$\mathbf{r}_0 = \mathbf{p}_0 + \mathbf{T}(\mathbf{u} + \mathbf{w}(\mathbf{u}, t)), \tag{1}$$

where $\mathbf{p}_0$ is the position vector of the track frame; $\mathbf{w}$ corresponds to the displacement vector due to the elastic deformation and small rigid body displacement of the solid; $\mathbf{T}$ is the rotation matrix that relations the trajectory frame of the track with the fixed frame.

Considering that the coordinate frame is chosen so that the wheelset spin rotation Ω is in the second axis $\mathbf{Y}_T$, the angular velocity tensor $\tilde{\mathbf{\Omega}}$ is defined as follows:

$$\tilde{\mathbf{\Omega}} = \begin{bmatrix} 0 & 0 & \Omega \\ 0 & 0 & 0 \\ -\Omega & 0 & 0 \end{bmatrix} = \Omega \mathbf{J}\text{; and } \mathbf{J} = \begin{bmatrix} 0 & 0 & 1 \\ 0 & 0 & 0 \\ -1 & 0 & 0 \end{bmatrix}. \tag{2}$$

The velocity due to the rigid body spinning is:

$$\mathbf{v} = \begin{pmatrix} v_1 & v_2 & v_3 \end{pmatrix}^{\mathrm{T}} = \tilde{\mathbf{\Omega}}\mathbf{u} = \Omega \mathbf{J}\mathbf{u} = \Omega \tilde{\mathbf{u}}, \tag{3}$$

where $\tilde{\mathbf{u}} = \begin{pmatrix} u_3 & 0 & -u_1 \end{pmatrix}^{\mathrm{T}}$. The velocity of the particle is computed through the material derivative of $\mathbf{r}_0$, and in the trajectory frame that is:

$$\begin{aligned} \frac{\mathrm{D}\mathbf{r}}{\mathrm{D}t} &= \mathbf{T}^{\mathrm{T}}\,\dot{\mathbf{p}}_0 + \mathbf{T}^{\mathrm{T}}\,\dot{\mathbf{T}}\,(\mathbf{u}+\mathbf{w}) + \dot{\mathbf{w}} + \sum_i v_i \frac{\partial \mathbf{u}}{\partial u_i} + \sum_i v_i \frac{\partial \mathbf{w}}{\partial u_i} \\ &= \dot{\mathbf{p}} + \tilde{\boldsymbol{\omega}}\,(\mathbf{u}+\mathbf{w}) + \dot{\mathbf{w}} + \Omega\,\mathbf{J}\,\mathbf{u} + \Omega \sum_i \tilde{u}_i \frac{\partial \mathbf{w}}{\partial u_i}, \end{aligned} \tag{4}$$

where $\dot{\mathbf{p}}$ is the speed of centre of the track frame (expressed in the trajectory frame) and $\tilde{\boldsymbol{\omega}} = \mathbf{T}^{\mathrm{T}}\,\dot{\mathbf{T}}$ the angular velocity matrix of the track frame. The two first velocity terms are associated to translational and rotational movement of the track frame, respectively; $\dot{\mathbf{w}}$ represents the velocity of the spatial point due to the flexibility; the term $\Omega\,\mathbf{J}\,\mathbf{u}$ is the velocity due to the rigid body spinning; and the last term is the convective velocity associated with the Eulerian coordinate system.

In order to obtain the expression of the kinetic energy for the wheelset, the square of the particle velocity is obtained, which reads:

$$\begin{aligned} \frac{\mathrm{D}\mathbf{r}^{\mathrm{T}}}{\mathrm{D}t}\frac{\mathrm{D}\mathbf{r}}{\mathrm{D}t} &= \dot{\mathbf{p}}^{\mathrm{T}}\,\dot{\mathbf{p}} + 2\dot{\mathbf{p}}^{\mathrm{T}}\,\tilde{\boldsymbol{\omega}}\,(\mathbf{u}+\mathbf{w}) + 2\Omega\dot{\mathbf{p}}^{\mathrm{T}}\,\mathbf{J}\,\mathbf{u} + 2\dot{\mathbf{p}}^{\mathrm{T}}\,\dot{\mathbf{w}} + 2\Omega\dot{\mathbf{p}}^{\mathrm{T}}\left(\sum_i \tilde{u}_i \frac{\partial \mathbf{w}}{\partial u_i}\right) \\ &\quad + \left(\mathbf{u}^{\mathrm{T}} + \mathbf{w}^{\mathrm{T}}\right)\tilde{\boldsymbol{\omega}}^{\mathrm{T}}\,\tilde{\boldsymbol{\omega}}\,(\mathbf{u}+\mathbf{w}) + 2\left(\mathbf{u}^{\mathrm{T}} + \mathbf{w}^{\mathrm{T}}\right)\tilde{\boldsymbol{\omega}}^{\mathrm{T}}\,\dot{\mathbf{w}} + 2\Omega\left(\mathbf{u}^{\mathrm{T}} + \mathbf{w}^{\mathrm{T}}\right)\tilde{\boldsymbol{\omega}}^{\mathrm{T}}\,\mathbf{J}\,\mathbf{u} \\ &\quad + 2\Omega\left(\sum_i \tilde{u}_i \frac{\partial \mathbf{w}^{\mathrm{T}}}{\partial u_i}\right)\tilde{\boldsymbol{\omega}}\,(\mathbf{u}+\mathbf{w}) + \dot{\mathbf{w}}^{\mathrm{T}}\,\dot{\mathbf{w}} + 2\Omega\dot{\mathbf{w}}^{\mathrm{T}}\,\mathbf{J}\,\mathbf{u} + 2\Omega\dot{\mathbf{w}}^{\mathrm{T}}\left(\sum_i \tilde{u}_i \frac{\partial \mathbf{w}}{\partial u_i}\right) \\ &\quad + \Omega^2\,\mathbf{u}^{\mathrm{T}}\,\mathbf{J}^{\mathrm{T}}\,\mathbf{J}\,\mathbf{u} + 2\Omega^2\left(\sum_i \tilde{u}_i \frac{\partial \mathbf{w}^{\mathrm{T}}}{\partial u_i}\right)\mathbf{J}\,\mathbf{u} + \Omega^2\left(\sum_i \tilde{u}_i \frac{\partial \mathbf{w}^{\mathrm{T}}}{\partial u_i}\right)\left(\sum_i \tilde{u}_i \frac{\partial \mathbf{w}}{\partial u_i}\right). \end{aligned} \tag{5}$$

Due to the geometry of revolution of the wheelset, the displacement vector $\mathbf{w}$ can be calculated through superposition of mode shapes in the non-rotating trajectory frame $\mathbf{X}_T\mathbf{Y}_T\mathbf{Z}_T$:

$$\mathbf{w}(\mathbf{u},t) = \mathbf{\Phi}(\mathbf{u})\,\mathbf{q}(t), \tag{6}$$

where $\mathbf{\Phi}(\mathbf{u})$ is the mode shape functions matrix of the free-boundary wheelset and $\mathbf{q}(t)$ is the Eulerian-modal coordinate vector. The small rigid body displacements of the solid are considered in this approach through the rigid body modes of the wheelset. It must be pointed out that the mode shape functions do not depend on time since the rotation of the solid does not change the mode shapes functions in spatial coordinates, because of the axial symmetry of the wheelset. In this study, 200 vibration modes of the wheelset have been considered, covering a frequency range up to 4.3 kHz, in order to obtain accurate results in the range of validity of the track model, which is up to 1.5 kHz. It should be noted that the wheelset is a very stiff and low damped solid, and consequently few modes above the maximum frequency of study are required to minimise errors due to modal truncation. Once the formula Eq. (6) is applied in Eq. (5), the kinetic energy results in the following expression:

$$\begin{aligned}
E_K = {} & \frac{1}{2}\int_{vol}\frac{\mathrm{D}\mathbf{r}^{\mathrm{T}}}{\mathrm{D}t}\frac{\mathrm{D}\mathbf{r}}{\mathrm{D}t}\rho\,\mathrm{d}v = \frac{1}{2}\dot{\mathbf{p}}^{\mathrm{T}}\dot{\mathbf{p}}\,m_w + \dot{\mathbf{p}}^{\mathrm{T}}\tilde{\mathbf{\omega}}\int_{vol}\rho\mathbf{u}\,\mathrm{d}v + \dot{\mathbf{p}}^{\mathrm{T}}\tilde{\mathbf{\omega}}\int_{vol}\rho\mathbf{\Phi}\,\mathrm{d}v\,\mathbf{q} + \Omega\dot{\mathbf{p}}^{\mathrm{T}}\mathbf{J}\int_{vol}\rho\mathbf{u}\,\mathrm{d}v \\
& + \dot{\mathbf{p}}^{\mathrm{T}}\int_{vol}\rho\mathbf{\Phi}\,\mathrm{d}v\,\dot{\mathbf{q}} + \Omega\dot{\mathbf{p}}^{\mathrm{T}}\int_{vol}\rho\left(\sum_i\tilde{u}_i\frac{\partial\mathbf{\Phi}}{\partial u_i}\right)\mathrm{d}v\,\mathbf{q} + \frac{1}{2}\int_{vol}\rho\mathbf{u}^{\mathrm{T}}\tilde{\mathbf{\omega}}^{\mathrm{T}}\tilde{\mathbf{\omega}}\mathbf{u}\,\mathrm{d}v \\
& + \int_{vol}\rho\mathbf{u}^{\mathrm{T}}\tilde{\mathbf{\omega}}^{\mathrm{T}}\tilde{\mathbf{\omega}}\mathbf{\Phi}\,\mathrm{d}v\,\mathbf{q} + \frac{1}{2}\mathbf{q}^{\mathrm{T}}\int_{vol}\rho\mathbf{\Phi}^{\mathrm{T}}\tilde{\mathbf{\omega}}^{\mathrm{T}}\tilde{\mathbf{\omega}}\mathbf{\Phi}\,\mathrm{d}v\,\mathbf{q} + \int_{vol}\rho\mathbf{u}^{\mathrm{T}}\tilde{\mathbf{\omega}}^{\mathrm{T}}\mathbf{\Phi}\,\mathrm{d}v\,\dot{\mathbf{q}} \\
& + \mathbf{q}^{\mathrm{T}}\int_{vol}\rho\mathbf{\Phi}^{\mathrm{T}}\tilde{\mathbf{\omega}}^{\mathrm{T}}\mathbf{\Phi}\,\mathrm{d}v\,\dot{\mathbf{q}} + \Omega\int_{vol}\rho\mathbf{u}^{\mathrm{T}}\tilde{\mathbf{\omega}}^{\mathrm{T}}\mathbf{J}\mathbf{u}\,\mathrm{d}v + \Omega\mathbf{q}^{\mathrm{T}}\int_{vol}\rho\mathbf{\Phi}^{\mathrm{T}}\tilde{\mathbf{\omega}}^{\mathrm{T}}\mathbf{J}\mathbf{u}\,\mathrm{d}v \\
& + \Omega\mathbf{q}^{\mathrm{T}}\int_{vol}\rho\left(\sum_i\tilde{u}_i\frac{\partial\mathbf{\Phi}^{\mathrm{T}}}{\partial u_i}\right)\tilde{\mathbf{\omega}}\mathbf{u}\,\mathrm{d}v + \Omega\mathbf{q}^{\mathrm{T}}\int_{vol}\rho\left(\sum_i\tilde{u}_i\frac{\partial\mathbf{\Phi}^{\mathrm{T}}}{\partial u_i}\right)\tilde{\mathbf{\omega}}\mathbf{\Phi}\,\mathrm{d}v\,\mathbf{q} \\
& + \frac{1}{2}\dot{\mathbf{q}}^{\mathrm{T}}\dot{\mathbf{q}} + \Omega\dot{\mathbf{q}}^{\mathrm{T}}\int_{vol}\rho\mathbf{\Phi}^{\mathrm{T}}\mathbf{J}\mathbf{u}\,\mathrm{d}v + \Omega\dot{\mathbf{q}}^{\mathrm{T}}\int_{vol}\rho\mathbf{\Phi}^{\mathrm{T}}\left(\sum_i\tilde{u}_i\frac{\partial\mathbf{\Phi}}{\partial u_i}\right)\mathrm{d}v\,\mathbf{q} \\
& + \frac{1}{2}\Omega^2\int_{vol}\rho\mathbf{u}^{\mathrm{T}}\mathbf{E}\mathbf{u}\,\mathrm{d}v + \Omega^2\mathbf{q}^{\mathrm{T}}\int_{vol}\rho\left(\sum_i\tilde{u}_i\frac{\partial\mathbf{\Phi}^{\mathrm{T}}}{\partial u_i}\right)\mathbf{J}\mathbf{u}\,\mathrm{d}v \\
& + \frac{1}{2}\Omega^2\mathbf{q}^{\mathrm{T}}\int_{vol}\rho\left(\sum_i\tilde{u}_i\frac{\partial\mathbf{\Phi}^{\mathrm{T}}}{\partial u_i}\right)\left(\sum_i\tilde{u}_i\frac{\partial\mathbf{\Phi}}{\partial u_i}\right)\mathrm{d}v\,\mathbf{q}.
\end{aligned} \tag{7}$$

Once the kinetic energy is known, the two terms of Lagrange's equation are computed as follows:

$$\left(\frac{\partial E_K}{\partial \mathbf{q}}\right)^{\mathrm{T}} = \int_{vol} \rho \boldsymbol{\Phi}^{\mathrm{T}}\,\mathrm{d}v\,\tilde{\boldsymbol{\omega}}^{\mathrm{T}}\,\dot{\mathbf{p}} + \Omega \int_{vol} \rho \left(\sum_i \tilde{u}_i \frac{\partial \boldsymbol{\Phi}^{\mathrm{T}}}{\partial u_i}\right)\mathrm{d}v\,\dot{\mathbf{p}} + \int_{vol} \rho \boldsymbol{\Phi}^{\mathrm{T}}\,\tilde{\boldsymbol{\omega}}^{\mathrm{T}}\,\tilde{\boldsymbol{\omega}}\,\mathbf{u}\,\mathrm{d}v$$
$$+ \int_{vol} \rho \boldsymbol{\Phi}^{\mathrm{T}}\,\tilde{\boldsymbol{\omega}}^{\mathrm{T}}\,\tilde{\boldsymbol{\omega}}\,\boldsymbol{\Phi}\,\mathrm{d}v\,\mathbf{q} + \int_{vol} \rho \boldsymbol{\Phi}^{\mathrm{T}}\,\tilde{\boldsymbol{\omega}}^{\mathrm{T}}\,\boldsymbol{\Phi}\,\mathrm{d}v\,\dot{\mathbf{q}} + \Omega \int_{vol} \rho \boldsymbol{\Phi}^{\mathrm{T}}\,\tilde{\boldsymbol{\omega}}^{\mathrm{T}}\,\mathbf{J}\,\mathbf{u}\,\mathrm{d}v$$
$$+ \Omega \int_{vol} \rho \left(\sum_i \tilde{u}_i \frac{\partial \boldsymbol{\Phi}^{\mathrm{T}}}{\partial u_i}\right)\tilde{\boldsymbol{\omega}}\,\mathbf{u}\,\mathrm{d}v + \Omega \int_{vol} \rho \left(\sum_i \tilde{u}_i \frac{\partial \boldsymbol{\Phi}^{\mathrm{T}}}{\partial u_i}\right)\tilde{\boldsymbol{\omega}}\,\boldsymbol{\Phi}\,\mathrm{d}v\,\mathbf{q} \tag{8}$$
$$+ \Omega \int_{vol} \rho \boldsymbol{\Phi}^{\mathrm{T}}\,\tilde{\boldsymbol{\omega}}^{\mathrm{T}} \left(\sum_i \tilde{u}_i \frac{\partial \boldsymbol{\Phi}}{\partial u_i}\right)\mathrm{d}v\,\mathbf{q} + \Omega \int_{vol} \rho \left(\sum_i \tilde{u}_i \frac{\partial \boldsymbol{\Phi}^{\mathrm{T}}}{\partial u_i}\right)\boldsymbol{\Phi}\,\mathrm{d}v\,\dot{\mathbf{q}}$$
$$+ \Omega^2 \int_{vol} \rho \left(\sum_i \tilde{u}_i \frac{\partial \boldsymbol{\Phi}^{\mathrm{T}}}{\partial u_i}\right)\mathbf{J}\,\mathbf{u}\,\mathrm{d}v + \Omega^2 \int_{vol} \rho \left(\sum_i \tilde{u}_i \frac{\partial \boldsymbol{\Phi}^{\mathrm{T}}}{\partial u_i}\right)\left(\sum_i \tilde{u}_i \frac{\partial \boldsymbol{\Phi}}{\partial u_i}\right)\mathrm{d}v\,\mathbf{q},$$

$$\frac{\mathrm{D}}{\mathrm{D}t}\left(\frac{\partial E_K}{\partial \dot{\mathbf{q}}}\right)^{\mathrm{T}} = \int_{vol} \rho \boldsymbol{\Phi}^{\mathrm{T}}\,\mathrm{d}v\,\ddot{\mathbf{p}} + \int_{vol} \rho \boldsymbol{\Phi}^{\mathrm{T}}\,\dot{\tilde{\boldsymbol{\omega}}}\,\mathbf{u}\,\mathrm{d}v + \int_{vol} \rho \boldsymbol{\Phi}^{\mathrm{T}}\,\dot{\tilde{\boldsymbol{\omega}}}\,\boldsymbol{\Phi}\,\mathrm{d}v\,\mathbf{q} + \int_{vol} \rho \boldsymbol{\Phi}^{\mathrm{T}}\,\tilde{\boldsymbol{\omega}}\,\boldsymbol{\Phi}\,\mathrm{d}v\,\dot{\mathbf{q}}$$
$$+ \ddot{\mathbf{q}} + \Omega \int_{vol} \rho \boldsymbol{\Phi}^{\mathrm{T}} \left(\sum_i \tilde{u}_i \frac{\partial \boldsymbol{\Phi}}{\partial u_i}\right)\mathrm{d}v\,\dot{\mathbf{q}} + \Omega \int_{vol} \rho \left(\sum_i \tilde{u}_i \frac{\partial \boldsymbol{\Phi}^{\mathrm{T}}}{\partial u_i}\right)\mathrm{d}v\,\dot{\mathbf{p}}$$
$$+ \Omega \int_{vol} \rho \left(\sum_i \tilde{u}_i \frac{\partial \boldsymbol{\Phi}^{\mathrm{T}}}{\partial u_i}\right)\tilde{\boldsymbol{\omega}}\,\mathbf{u}\,\mathrm{d}v + \Omega \int_{vol} \rho \boldsymbol{\Phi}^{\mathrm{T}}\,\tilde{\boldsymbol{\omega}}\,\mathbf{J}\,\mathbf{u}\,\mathrm{d}v$$
$$+ \Omega \int_{vol} \rho \left(\sum_i \tilde{u}_i \frac{\partial \boldsymbol{\Phi}^{\mathrm{T}}}{\partial u_i}\right)\tilde{\boldsymbol{\omega}}\,\boldsymbol{\Phi}\,\mathrm{d}v\,\mathbf{q} + \Omega \int_{vol} \rho \boldsymbol{\Phi}^{\mathrm{T}}\,\tilde{\boldsymbol{\omega}} \left(\sum_i \tilde{u}_i \frac{\partial \boldsymbol{\Phi}}{\partial u_i}\right)\mathrm{d}v\,\mathbf{q}$$
$$+ \Omega^2 \int_{vol} \rho \left(\sum_i \tilde{u}_i \frac{\partial \boldsymbol{\Phi}^{\mathrm{T}}}{\partial u_i}\right)\mathbf{J}\,\mathbf{u}\,\mathrm{d}v - \Omega^2 \int_{vol} \rho \boldsymbol{\Phi}^{\mathrm{T}}\,\mathbf{E}\,\mathbf{u}\,\mathrm{d}v$$
$$+ \Omega^2 \int_{vol} \rho \left(\sum_i \tilde{u}_i \frac{\partial \boldsymbol{\Phi}^{\mathrm{T}}}{\partial u_i}\right)\left(\sum_i \tilde{u}_i \frac{\partial \boldsymbol{\Phi}}{\partial u_i}\right)\mathrm{d}v\,\mathbf{q} - \Omega^2 \int_{vol} \rho \boldsymbol{\Phi}^{\mathrm{T}} \left(\sum_{i=1,3} u_i \frac{\partial \boldsymbol{\Phi}}{\partial u_i}\right)\mathrm{d}v\,\mathbf{q}$$
$$+ \Omega^2 \int_{vol} \rho \boldsymbol{\Phi}^{\mathrm{T}} \left(\sum_i \sum_j \tilde{u}_i\,\tilde{u}_j \frac{\partial^2 \boldsymbol{\Phi}}{\partial u_i\,\partial u_j}\right)\mathrm{d}v\,\mathbf{q}, \tag{9}$$

with $\mathbf{E} = -\mathbf{J}\,\mathbf{J} = \begin{bmatrix} 1 & 0 & 0 \\ 0 & 0 & 0 \\ 0 & 0 & 1 \end{bmatrix}$.

The equation of motion of the flexible and rotating wheelset is derived by means of Lagrange's equation. Considering Eqs. (8) and (9) and taking into account that matrix $\tilde{\boldsymbol{\omega}}$ is anti-symmetric, the following equation is obtained:

$$
\begin{aligned}
&\ddot{\mathbf{q}} + \left[2\Omega \int_{vol} \rho \boldsymbol{\Phi}^{\mathrm{T}} \left(\sum_i \tilde{u}_i \frac{\partial \boldsymbol{\Phi}}{\partial u_i} \right) \mathrm{d}v + 2 \int_{vol} \rho \boldsymbol{\Phi}^{\mathrm{T}} \tilde{\boldsymbol{\omega}} \boldsymbol{\Phi} \, \mathrm{d}v \right] \dot{\mathbf{q}} \\
&+ \left[\Omega^2 \int_{vol} \rho \boldsymbol{\Phi}^{\mathrm{T}} \left(\sum_i \sum_j \tilde{u}_i \tilde{u}_j \frac{\partial^2 \boldsymbol{\Phi}}{\partial u_i \partial u_j} \right) \mathrm{d}v - \Omega^2 \int_{vol} \rho \boldsymbol{\Phi}^{\mathrm{T}} \left(\sum_{i=1,3} u_i \frac{\partial \boldsymbol{\Phi}}{\partial u_i} \right) \mathrm{d}v \right. \\
&\left. + 2\Omega \int_{vol} \rho \boldsymbol{\Phi}^{\mathrm{T}} \tilde{\boldsymbol{\omega}} \left(\sum_i \tilde{u}_i \frac{\partial \boldsymbol{\Phi}}{\partial u_i} \right) \mathrm{d}v + \int_{vol} \rho \boldsymbol{\Phi}^{\mathrm{T}} \dot{\tilde{\boldsymbol{\omega}}} \boldsymbol{\Phi} \, \mathrm{d}v - \int_{vol} \rho \boldsymbol{\Phi}^{\mathrm{T}} \tilde{\boldsymbol{\omega}}^{\mathrm{T}} \tilde{\boldsymbol{\omega}} \boldsymbol{\Phi} \, \mathrm{d}v \right] \mathbf{q} \\
&= \Omega^2 \int_{vol} \rho \boldsymbol{\Phi}^{\mathrm{T}} \mathbf{E} \mathbf{u} \, \mathrm{d}v - 2\Omega \int_{vol} \rho \boldsymbol{\Phi}^{\mathrm{T}} \tilde{\boldsymbol{\omega}} \mathbf{J} \mathbf{u} \, \mathrm{d}v - \int_{vol} \rho \boldsymbol{\Phi}^{\mathrm{T}} \dot{\tilde{\boldsymbol{\omega}}} \mathbf{u} \, \mathrm{d}v \\
&+ \int_{vol} \rho \boldsymbol{\Phi}^{\mathrm{T}} \tilde{\boldsymbol{\omega}}^{\mathrm{T}} \tilde{\boldsymbol{\omega}} \mathbf{u} \, \mathrm{d}v - \int_{vol} \rho \boldsymbol{\Phi}^{\mathrm{T}} \, \mathrm{d}v \mathbf{T}^{\mathbf{T}} \ddot{\mathbf{p}}_0 + \mathbf{Q}.
\end{aligned}
\tag{10}
$$

The modal properties are computed from a finite element (FE) model, therefore it is adequate to use the FE methodology for computing the equation of motion numerically. The mode shape functions are obtained into the *e*-th element of the FE mesh as follows:

$$
\boldsymbol{\Phi}(\mathbf{u}) = \mathbf{N}^e(\mathbf{u}) \boldsymbol{\Phi}^e_{FE}, \tag{11}
$$

where $\mathbf{N}^e(\mathbf{u})$ is the basis (or shape) function matrix of the *e*-th element, and $\boldsymbol{\Phi}^e_{\mathrm{FE}}$ the mode shapes computed in the nodes of the *e*-th element through the FE model.

This approach allows obtaining the matrices of the equation of motion by means of the matrices of the elements. These matrices have to be assembled in global matrices by following the standard FE assembling technique. The first matrix in Eq. (10) is obtained by means of the approach in Eq. (11) as follows:

$$
\begin{aligned}
\tilde{\mathbf{V}} &= \int_{vol} \rho \boldsymbol{\Phi}^{\mathrm{T}} \left(\sum_i \tilde{u}_i \frac{\partial \boldsymbol{\Phi}}{\partial u_i} \right) \mathrm{d}v = \sum_{e=1}^{n_e} \int_{vol^e} \rho \boldsymbol{\Phi}^{e\,\mathrm{T}}_{\mathrm{FE}} \mathbf{N}^{e\,\mathrm{T}} \left(\sum_i \tilde{u}_i \frac{\partial \mathbf{N}^e}{\partial u_i} \right) \boldsymbol{\Phi}^e_{\mathrm{FE}} \, \mathrm{d}v \\
&= \boldsymbol{\Phi}^{\mathrm{T}}_{\mathrm{FE}} \left(\sum_{e=1}^{n_e} \int_{vol^e} \rho \mathbf{N}^{e\,\mathrm{T}} \left(\sum_i \tilde{u}_i \frac{\partial \mathbf{N}^e}{\partial u_i} \right) \mathrm{d}v \right) \boldsymbol{\Phi}_{\mathrm{FE}},
\end{aligned}
\tag{12}
$$

where n_e is the number of elements in the FE mesh, *vol* is the volume domain associated with the undeformed solid, and vol^e is the volume of the *e*-th element.

Defining the *e*-th element matrtix $\mathbf{V}^e$ as:

$$
\mathbf{V}^e = \int_{vol^e} \rho \mathbf{N}^{e\,\mathrm{T}} \left(\sum_i \tilde{u}_i \frac{\partial \mathbf{N}^e}{\partial u_i} \right) \mathrm{d}v \tag{13}
$$

the following compact expression of $\tilde{\mathbf{V}}$ is obtained:

$$\tilde{\mathbf{V}} = \mathbf{\Phi}_{\mathrm{FE}}^{\mathrm{T}} \left(\sum_{e=1}^{n_e} \mathbf{V}^e \right) \mathbf{\Phi}_{\mathrm{FE}} \tag{14}$$

Following the same procedure as in Eq. (12), the remaining matrices of the equation of motion are obtained:

$$\mathbf{P}^e = \int_{vol^e} \rho \mathbf{N}^{e\mathrm{T}} \tilde{\boldsymbol{\omega}} \mathbf{N}^e \, \mathrm{d}v \,, \; \tilde{\mathbf{P}} = \mathbf{\Phi}_{\mathrm{FE}}^{\mathrm{T}} \left(\sum_{e=1}^{n_e} \mathbf{P}^e \right) \mathbf{\Phi}_{\mathrm{FE}} \,, \tag{15}$$

$$\mathbf{A}^e = \int_{vol^e} \rho \mathbf{N}^{e\mathrm{T}} \left(\sum_i \sum_j \tilde{u}_i \, \tilde{u}_j \frac{\partial^2 \mathbf{N}^e}{\partial u_i \, \partial u_j} \right) \mathrm{d}v \,, \; \tilde{\mathbf{A}} = \mathbf{\Phi}_{\mathrm{FE}}^{\mathrm{T}} \left(\sum_{e=1}^{n_e} \mathbf{A}^e \right) \mathbf{\Phi}_{\mathrm{FE}} \,, \tag{16}$$

$$\mathbf{C}^e = \int_{vol^e} \rho \mathbf{N}^{e\mathrm{T}} \left(\sum_{i=1,3} u_i \frac{\partial \mathbf{N}^e}{\partial u_i} \right) \mathrm{d}v \,, \; \tilde{\mathbf{C}} = \mathbf{\Phi}_{\mathrm{FE}}^{\mathrm{T}} \left(\sum_{e=1}^{n_e} \mathbf{C}^e \right) \mathbf{\Phi}_{\mathrm{FE}} \,, \tag{17}$$

$$\mathbf{S}^e = \int_{vol^e} \rho \mathbf{N}^{e\mathrm{T}} \tilde{\boldsymbol{\omega}} \left(\sum_i \tilde{u}_i \frac{\partial \mathbf{N}^e}{\partial u_i} \right) \mathrm{d}v \,, \; \tilde{\mathbf{S}} = \mathbf{\Phi}_{\mathrm{FE}}^{\mathrm{T}} \left(\sum_{e=1}^{n_e} \mathbf{S}^e \right) \mathbf{\Phi}_{\mathrm{FE}} \,, \tag{18}$$

$$\mathbf{R}^e = \int_{vol^e} \rho \mathbf{N}^{e\mathrm{T}} \dot{\tilde{\boldsymbol{\omega}}} \mathbf{N}^e \, \mathrm{d}v \,, \; \tilde{\mathbf{R}} = \mathbf{\Phi}_{\mathrm{FE}}^{\mathrm{T}} \left(\sum_{e=1}^{n_e} \mathbf{R}^e \right) \mathbf{\Phi}_{\mathrm{FE}} \,, \tag{19}$$

$$\mathbf{B}^e = \int_{vol^e} \rho \mathbf{N}^{e\mathrm{T}} \tilde{\boldsymbol{\omega}}^{\mathrm{T}} \tilde{\boldsymbol{\omega}} \mathbf{N}^e \, \mathrm{d}v \,, \; \tilde{\mathbf{B}} = \mathbf{\Phi}_{\mathrm{FE}}^{\mathrm{T}} \left(\sum_{e=1}^{n_e} \mathbf{B}^e \right) \mathbf{\Phi}_{\mathrm{FE}} \,, \tag{20}$$

$$\mathbf{c}^e = \int_{vol^e} \rho \mathbf{N}^{e\mathrm{T}} \mathbf{E} \mathbf{u} \, \mathrm{d}v \,, \; \tilde{\mathbf{c}} = \mathbf{\Phi}_{\mathrm{FE}}^{\mathrm{T}} \left(\sum_{e=1}^{n_e} \mathbf{c}^e \right) , \tag{21}$$

$$\mathbf{U}^e = \int_{vol^e} \rho \mathbf{N}^{e\mathrm{T}} \tilde{\boldsymbol{\omega}} \mathbf{J} \mathbf{u} \, \mathrm{d}v \,, \; \tilde{\mathbf{U}} = \mathbf{\Phi}_{\mathrm{FE}}^{\mathrm{T}} \left(\sum_{e=1}^{n_e} \mathbf{U}^e \right) , \tag{22}$$

$$\mathbf{H}^e = \int_{vol^e} \rho \mathbf{N}^{e\mathrm{T}} \dot{\tilde{\boldsymbol{\omega}}} \mathbf{u} \, \mathrm{d}v \,, \; \tilde{\mathbf{H}} = \mathbf{\Phi}_{\mathrm{FE}}^{\mathrm{T}} \left(\sum_{e=1}^{n_e} \mathbf{H}^e \right) , \tag{23}$$

$$\mathbf{N}^e = \int_{vol^e} \rho \mathbf{N}^{e\mathrm{T}} \tilde{\boldsymbol{\omega}}^{\mathrm{T}} \tilde{\boldsymbol{\omega}} \mathbf{u} \, \mathrm{d}v \,, \; \tilde{\mathbf{N}} = \mathbf{\Phi}_{\mathrm{FE}}^{\mathrm{T}} \left(\sum_{e=1}^{n_e} \mathbf{N}^e \right) , \tag{24}$$

$$\mathbf{G}^e = \int_{vol^e} \rho \mathbf{N}^{e\mathrm{T}} \, \mathrm{d}v \,, \; \tilde{\mathbf{G}} = \mathbf{\Phi}_{\mathrm{FE}}^{\mathrm{T}} \left(\sum_{e=1}^{n_e} \mathbf{G}^e \right) \mathbf{T}^{\mathbf{T}} \ddot{\mathbf{p}}_0 \,, \tag{25}$$

resulting the following equation of motion for the flexible wheelset running along a curved track:

$$\ddot{\mathbf{q}} + \left(2\,\Omega\,\tilde{\mathbf{V}} + 2\,\tilde{\mathbf{P}}\right)\dot{\mathbf{q}} + \left(\Omega^2\left(\tilde{\mathbf{A}} - \tilde{\mathbf{C}}\right) + 2\,\Omega\,\tilde{\mathbf{S}} + \tilde{\mathbf{R}} - \tilde{\mathbf{B}} + \tilde{\mathbf{D}}\right)\mathbf{q} = \Omega^2\,\tilde{\mathbf{c}} - 2\,\Omega\,\tilde{\mathbf{U}} - \tilde{\mathbf{H}} + \tilde{\mathbf{N}} - \tilde{\mathbf{G}} + \mathbf{Q}_c + \mathbf{Q}_s . \qquad (26)$$

where:

- matrices $\tilde{\mathbf{V}}$ and $\tilde{\mathbf{P}}$ are associated with the inertial force due to Coriolis acceleration originated by the rotations of the wheelset and track frames, respectivelly;
- matrix $\tilde{\mathbf{A}}$ is related to the force due to the convective acceleration;
- $\tilde{\mathbf{C}}$ is the centrifugal stiffening matrix;
- matrix $\tilde{\mathbf{S}}$ introduces the inertial force due to the convective velocity and the angular velocity of the track frame;
- matrix $\tilde{\mathbf{R}}$ takes into account the force due to the tangential acceleration of the track frame that is associated with the deformed configuration;
- matrix $\tilde{\mathbf{B}}$ considers the centrifugal effect due to the deformation of the solid that is associated with the track frame rotation;
- $\tilde{\mathbf{D}}$ is the wheelset modal stiffness matrix, a diagonal matrix formed by the squares of the undamped natural frequencies of the free-boundary wheelset;
- vector $\tilde{\mathbf{c}}$ is the modal force due to the centrifugal effect associated with the wheel rotation in the undeformed configuration;
- vector $\tilde{\mathbf{U}}$ contains the constant forces associated with Coriolis effect;
- vector $\tilde{\mathbf{H}}$ accounts for the forces due to the tangential acceleration of the track frame that is associated with the undeformed configuration;
- $\tilde{\mathbf{N}}$ is the generalised force vector of the centrifugal forces related to track frame rotation;
- vector $\tilde{\mathbf{G}}$ accounts for the centrifugal effects associated with the translation motion of the track frame;
- vectors $\mathbf{Q}_c$ and $\mathbf{Q}_s$ contain the generalized forces acting on the flexible wheelset resulting respectively from wheel-rail contact forces (see Section 4) and from the forces applied by the primary suspension (see Section 2.2).

2.2. Boundary conditions

While running through a curve, the wheelset develops steady-state values of the creepages and contact forces that are substantially different from the case of tangent track running. On account of the non-linearity of wheel-rail contact, these steady-state contact forces and creepages strongly affect the coupled wheelset - track dynamics in the entire frequency range addressed by the study, and therefore need to be properly taken into account in the numerical simulation procedure. It is

also worth noticing that the elastic coupling of different wheelsets in the vehicle, typically via the primary suspensions and bogie frame, affects the steady-state contact forces and creepages in the curve.

The approach followed in the paper is to consider one single wheelset and to reproduce the steady-state curving effects by prescribing appropriate forces at the primary suspension: these forces are derived from the results of a low-frequency multi-body simulation in which the whole vehicle is considered, but all bodies are assumed to behave as rigid. Compared to considering the complete bogie with two flexible wheelsets, this approach allows to reduce substantially the time required for the simulation, because the additional degrees of freedom of the second wheelset and of the bogie frame are not included in the analysis, and also because the time consuming procedure required to evaluate the contact forces at each time step is carried out for two wheels instead of four, whereas the low-frequency simulation of the whole vehicle requires a very short simulation time, on account of the assumption of neglecting the flexibility of all bodies.

The low frequency multi-body simulation is performed using software ADTreS developed at Politecnico di Milano [12] and considers a vehicle formed by one carbody, two bogies and four wheelsets. Given that the interest of the rigid body simulation is only to derive the steady-state curving condition for the vehicle, no effect of track irregularity or wheel imperfections is considered in this simulation.

In order to ensure that the contact forces and creepages are correctly initialised, the steady-state forces applied on the wheelset at the axle-boxes via the primary suspension along the $\mathbf{Z}_T$ and $\mathbf{Y}_T$ axes of the trajectory coordinate frame are prescribed in Eq. (26) to match the values obtained in the low-frequency simulation: in this way, the steady state $\mathbf{Z}_T$ component of the contact forces on the two wheels and the sum of the steady-state contact forces along the $\mathbf{Y}_T$ axis are correctly reproduced by the flexible wheelset-track model. Furthermore, the longitudinal stiffness of the primary suspension is introduced in Eq. (26) and the longitudinal displacements (i.e. directed along axis $\mathbf{X}_T$) of the bogie at the primary suspension are prescribed to match the values obtained from the low-frequency simulation. By doing so, the steady-state longitudinal and lateral creep forces on both wheels are correctly initialised in the high-frequency model. As shown in Section 5, cf. comments to Table 2, this procedure allows to obtain a very good agreement of the steady state forces for the rigid body model of the complete vehicle and for the model of the single flexible wheelset.

Table 1: Simulation parameters

Wheelset model data		**Track model data**	
Mass of wheelset	1375 kg	Sleeper bay	0.6 m
Axle load	120 kN	Sleeper number	70
Primary suspension longitudinal stiffness	7.5 MN/m	Sleeper mass	324 kg
Primary suspension lateral stiffness	7.1 MN/m	Track bed stiffness	200 MN/m
Primary suspension vertical stiffness	0.81 MN/m	Track bed damping	150 kNs/m
Primary suspension longitudinal damping	100 kNs/m	Rail pad stiffness	1 GN/m
Primary suspension lateral damping	100 kNs/m	Rail pad damping	50 kNs/m
Primary suspension vertical damping	30 kNs/m	Rail section	UIC60

Table 2: Steady-state wheel-rail contact forces for the rigid multi-body model of the entire vehicle and for the single flexible wheelset model.

	Outer wheel		Inner wheel	
	Rigid multi-body model	Flexible wheelset model	Rigid multi-body model	Flexible wheelset model
Vertical force	69.57 kN	70.01 kN	49.82 kN	49.71 kN
Lateral force	5,68 kN	5,91 kN	-3,75 kN	-3,99 kN
Longitudinal force	14.39 kN	15.16 kN	-14.39 kN	-15.16 kN

All the above described boundary conditions are applied on the flexible wheelset model Eq. (26) by appropriately setting the terms in vector $\mathbf{Q}_s$. These consist of the generalised forces associated with the modal coordinates $\mathbf{q}$ of the concentrated forces applied at the axle-box seats, defined as explained above in this section.

3. THE TRACK MODEL

The track model has been adapted from the one presented in reference [13] where cyclic boundary conditions were adopted. With respect to this previous work, here different sleeper bay distances have been considered in order to take into account the dynamics of a constant radius curved track.

The cyclic track approach that is used in the present paper models a circumferential constant radius track negotiated by a set of identical vehicles, uniformly distributed in such a way that each vehicle

is set at a constant distance L apart from the adjacent ones and travel at the same velocity V, see Fig. 2. The constant distance L is set large enough to avoid the dynamic interaction between the vehicles and cyclic boundary conditions are introduced at the ends of the model. Hence, due to the periodicity of the structure and of the loading conditions, the study of the track is reduced to a single section having finite length L.

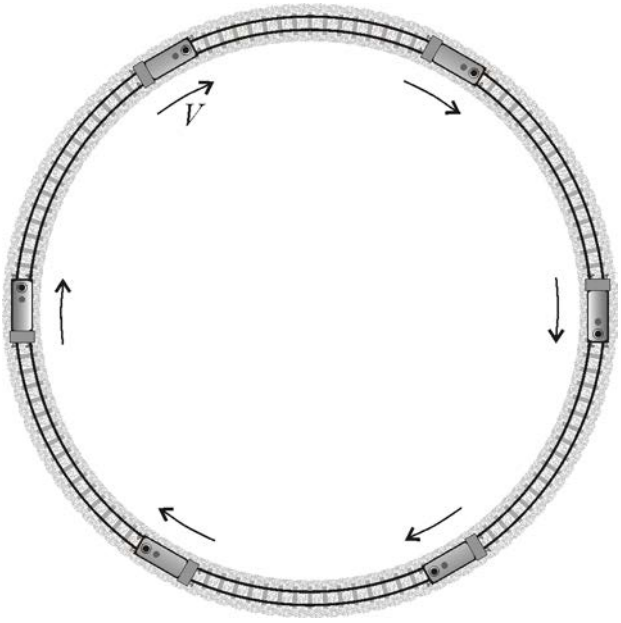

Figure 2: The cyclic track model.

The approach adopts a substructuring technique where rails and sleepers are treated separately. The rails are modelled as Timoshenko beams, including bending deformations in vertical/lateral directions, as well as torsional deformations. Since the model addresses curves with radius in the range of hundreds of meters or larger, the curvature of the rails is neglected in the beam formulation.

Rail vibration is introduced in terms of modal superposition for the unconstrained rail with cyclic boundary conditions, hence resulting into a set of de-coupled 1-dof equations. According to [1], the rail model base on one single Timoshenko beam is valid up to 1.5 kHz for lateral rail vibration and up to 2 kHz in vertical for vertical vibration. Given that lateral rail vibration is important for wheelset track interaction in curve, it is assumed that the frequency range of validity for the track model is 1.5 kHz approximately. In order to minimise errors caused by modal truncation, all the rails modes of vibration falling in the range below 8 kHz were considered. A procedure for obtaining an optimised number of modes was proposed in Ref. [13].

The discrete rail supports are introduced in the form of lumped parameter systems. The rail pads are modelled as lumped visco-elastic elements generating the interaction forces between the rails and the sleepers, represented as lumped masses. Ballast dynamics is neglected here, being not relevant

for the dynamic behaviour of the wheelset, but the equivalent ballast stiffness and damping are accounted for by means of lumped spring and dashpot elements connected to the sleepers.

The lateral and vertical displacements of the rail axis are [13]:

$$w^y(x,t) = \sum_r W_r^y(x)\, q_r^y(t), \tag{27}$$

$$w^z(x,t) = \sum_r W_r^z(x)\, q_r^z(t), \tag{28}$$

and the torsion and the rotations of the rail's cross-section are:

$$\psi^x(x,t) = \sum_r \Psi_r^x(x)\, q_r^x(t), \tag{29}$$

$$\psi^y(x,t) = \sum_r \Psi_r^y(x)\, q_r^z(t), \tag{30}$$

$$\psi^z(x,t) = \sum_r \Psi_r^z(x)\, q_r^y(t), \tag{31}$$

where $W_r^y(x)$, $W_r^z(x)$, $\Psi_r^x(x)$, $\Psi_r^y(x)$ and $\Psi_r^z(x)$ are the r-th modal functions of the Timoshenko periodic beam, and $q_r^x(t)$, $q_r^y(t)$ and $q_r^z(t)$ are the modal coordinates associated with torsional, lateral and vertical rail vibrations, respectively.

The resulting r-th equation of motion for the cyclic track model in modal coordinates take the form:

$$\ddot{q}_r + 2\,\xi_r\,\omega_r\,\dot{q}_r + \omega_r^2\,q_r = f_r\,, \tag{32}$$

being ω_r the r-th undamped frequency and ξ_r the modal damping. The modal forces f_r are computed from the wheel rail contact forces acting on the track.

In this way, the displacements of the rail in the present contact point can be evaluated from the displacements and rotations of the rail axis as follows:

$$\mathbf{x}_{r,j} = \mathbf{E}_j \begin{pmatrix} w_j^y & w_j^z & \psi_j^x & \psi_j^y & \psi_j^z \end{pmatrix}^{\mathrm{T}}, \tag{33}$$

where $\mathbf{x}_{r,j}$ is the vector of contact point displacements in j-th rail, and the matrix $\mathbf{E}_j$ relates the displacements in rail axis and contact points.

4. THE MODEL OF THE WHEEL-RAIL CONTACT FORCES

Eqs. (26) and (32) are coupled by the wheel-rail contact forces, which can be defined as a function of the wheelset modal coordinates $\mathbf{q}$ and their time derivatives $\dot{\mathbf{q}}$ and of the track displacements $\mathbf{x}_r$ together with their time derivatives $\dot{\mathbf{x}}_r$. The calculation of the contact forces is performed within the time step integration of the equations of motion for the wheelset and the track. First the motion (position and velocity) of the contact points on wheel and rail surfaces is determined, then the normal and tangential wheel-rail contact forces are computed as a function of the relative wheel-rail motion at the contact point, finally the generalised forces on the vehicle and track coordinates are defined based on the principle of virtual work.

4.1 Contact kinematics

Using the modal superposition principle, the vectors $\mathbf{r}_{w,j}$ of the wheel displacements at the contact point (with j = 1,2 representing the left and right wheel) are computed as:

$$\mathbf{r}_{w,j} = \boldsymbol{\Phi}\left(\mathbf{u}_{w,j}\right)\mathbf{q}(t) + \mathbf{r}_{w,j}^{(irr)}(t), \tag{34}$$

with $\mathbf{u}_{w,j}$ the position of the contact point on the wheel and $\mathbf{r}_{w,j}^{(irr)}$ a vector accounting for the effect of wheel out-of-roundness, which is defined as a periodical function of time. In the same way, the "material velocity" vectors $\dot{\mathbf{r}}_{w,j}^{(M)}$ of the wheel at the contact point, i.e. the velocity of the material point on each wheel instantaneously in contact with the rail are defined as:

$$\dot{\mathbf{r}}_{w,j}^{(M)} = \boldsymbol{\Phi}\left(\mathbf{u}_{w,j}\right)\dot{\mathbf{q}}(t) + \Omega\left(\sum_i \tilde{u}_i \frac{\partial \boldsymbol{\Phi}}{\partial u_i}\right)\mathbf{q}(t). \tag{35}$$

The rail displacements at the contact points on the left and right rails $\mathbf{r}_{r,j}$ are obtained according to the following expression:

$$\mathbf{r}_{r,j} = \mathbf{x}_{r,j}(t) + \mathbf{r}_{r,j}^{(irr)}(t), \tag{36}$$

where $\mathbf{r}_{r,j}^{(irr)}$ is a vector accounting for the effect of geometric imperfections in the track due to irregularity and rail roughness, whereas the material velocity of the rails at the contact points is computed as:

$$\dot{\mathbf{r}}_{r,j}^{(M)} = \dot{\mathbf{x}}_{r,j}^{(M)} = \mathbf{E}_j \begin{pmatrix} \dot{w}_j^y & \dot{w}_j^z & \dot{\psi}_j^x & \dot{\psi}_j^y & \dot{\psi}_j^z \end{pmatrix}^{\mathrm{T}} + V\,\mathbf{E}_j \frac{\partial}{\partial x}\begin{pmatrix} w_j^y & w_j^z & \psi_j^x & \psi_j^y & \psi_j^z \end{pmatrix}^{\mathrm{T}}, \tag{37}$$

being V the speed of the wheelset.

4.2 Calculation of wheel-rail contact forces

The model of wheel-rail contact used to reproduce the dynamic coupling between the vehicle and the track is a pre-tabulated, multi-Hertzian one [14]. Prior to the simulation, wheel-rail contact geometry is processed starting from measured or theoretical wheel and rail profiles and the contact parameters required to compute wheel-rail contact forces are stored in a contact table. According to this procedure, the change in the location of the contact point due to the instantaneous deformation of the wheelset is neglected in the calculation of the contact forces. This simplification is justified because the magnitude of the elastic wheel deformation (in the order of $1 - 10\ 10^{-5}$ m) is much smaller than the rigid lateral movement of the wheelset relative to the track, which is between $5\ 10^{-3}$ and 10^{-2} m, depending on the track gauge, rail profiles, wheel profile.

An alternative approach would be to compute the position of the contact point and the contact parameters at each time step of the numerical integration, considering also the deformation of the wheelset as in [9]. However, this approach would entail a much more CPU intensive calculation, whereas the focus in this work is to keep the computational effort as low as possible, while retaining in the model the main effects of wheelset flexibility for the problem studied.

The parameters stored in the contact table are the contact angle, the variation of the wheel rolling radius with respect to the nominal one, the curvatures of the wheel and rail profiles in the contact point region and an undeformed distance which is equal to zero for the geometric contact point and greater than zero for the other potential contact points. More details on the process used to derive the contact table can be found in [15], note that with respect to the theory presented there, in this work the effect of the angle of attack is neglected, thus leading to a simplified planar contact problem. This assumption is reasonable on account of the fact that only large radius curves are considered in this research.

In order to compute the contact forces at time *t*, the relative wheel-rail lateral displacement is computed and the contact tables are interpolated, finding the contact parameters for one or more wheel-rail potential contact points. Then, for each *i*-th potential contact point of the *j*-th wheel-rail couple the so-called “normal problem” is solved. To this aim, an elastic penetration is computed by projecting the relative wheel-rail displacements in the contact point along the direction normal to the contact plane, which is defined by the contact angle parameter in the contact table. To consider the change with time of the normal direction, the penetration is computed according to an incremental definition, so that the penetration $p_{i,j}^{(t)}$ at time t is defined as the sum of the penetration at the previous time step $t-\Delta t$ plus the penetration increment from the previous to the present time step:

$$p_{i,j}^{(t)} = p_{i,j}^{(t-\Delta t)} + \mathbf{n}_i^T \left(\left(\mathbf{r}_{w,j}^{(t)} - \mathbf{r}_{w,j}^{(t-\Delta t)} \right) - \left(\mathbf{r}_{r,j}^{(t)} - \mathbf{r}_{r,j}^{(t-\Delta t)} \right) \right) - \left(\delta_{i,j}^{(t)} - \delta_{i,j}^{(t-\Delta t)} \right), \tag{38}$$

where $\mathbf{n}_i$ is the vector defining the normal direction for the *i*-th contact, $\delta_{i,j}$ is the undeformed distance for the *i*-th contact of the *j*-th wheel-rail couple, and superscripts "*(t)*" and "*(t-Δt)*" denote quantities evaluated at the present and previous time step respectively.

The normal force $N_{i,j}^{(t)}$ is computed as function of the elastic penetration according to Hertz's formulae using the profile curvatures retrieved from the contact table:

$$\begin{cases} N_{i,j}^{(t)} = 0 & \text{if} \quad p_{i,j}^{(t)} \le 0 \\ N_{i,j}^{(t)} = C_{i,j} \left(p_{i,j}^{(t)} \right)^{\frac{3}{2}} & \text{if} \quad p_{i,j}^{(t)} > 0 \end{cases}. \tag{39}$$

The creep forces are then computed as function of the creepages, according to the heuristic formulae by Shen et al. [16]. The longitudinal and transversal creepages, $\varepsilon_{L_{i,j}}$ and $\varepsilon_{T_{i,j}}$ respectively, are computed as follows:

$$\varepsilon_{L_{i,j}} = \frac{\mathbf{l}_i^T \left(\dot{\mathbf{r}}_{w,j}^{(M)} - \dot{\mathbf{r}}_{r,j}^{(M)} \right)}{V} - \frac{\Delta R_{i,j}}{R_0} + \frac{s}{R_0} (-1)^j, \tag{40}$$

$$\varepsilon_{T_{i,j}} = \frac{\mathbf{t}_i^T \left(\dot{\mathbf{r}}_{w,j}^{(M)} - \dot{\mathbf{r}}_{r,j}^{(M)} \right)}{V} - \sigma_j \cos\left(\gamma_j \right), \tag{41}$$

with $\mathbf{l}_i$ and $\mathbf{t}_i$ the vectors defining the longitudinal and transversal direction for the *i*-th contact, R_0 the radius of the curve, V the speed of the wheelset, $\Delta R_{i,j}$ the rolling radius variation for the contact point under consideration, σ_j the angle of attack of the wheel, s half-distance between the wheel nominal running circles and γ_j the contact angle of the wheel at the actual contact point.

Finally, the normal and creep forces obtained at each *i*-th wheel-rail contact point are projected along the trajectory frame $\mathbf{X}_T\mathbf{Y}_T\mathbf{Z}_T$ and summed over all active contacts occurring in the same wheel-rail couple, and the components of the resulting contact forces along the modal coordinates $\mathbf{q}$ are derived by standard application of the principle of virtual work, providing vector $\mathbf{Q}_c$ in Eq. (26).

5. RESULTS

In this section, results of wheelset-track interaction simulations are presented considering different sources of excitation: a single harmonic rail corrugation, random rail roughness and a wheelflat. Results are also presented for a rigid wheelset model, i.e. including in the modal synthesis only the

rigid modes of vibration of the unconstrained wheelset. In this way, the effect of wheelset flexibility is pointed out. Furthermore, for the wheelflat excitation case, results are also presented for the wheelset running at the same speed in tangent track, to assess the effect of curving on high-frequency wheelset-track interaction, which is the main innovation introduced in this paper.

The case study considered here refers to the trailed car of a concentrated power train for high-speed passenger service. The vehicle is equipped with a solid axle wheelset with monobloc, light design wheels. The track considered features UIC60 rails and track parameters are based on the EUROBALT project [17], considering a "stiff" track. Table 1 summarises the input data used to set-up the simulation model.

All simulation cases presented below consider the wheelset running at 150 km/h through a curve with radius 1000 m and a track cant equal to 150 mm. For this running condition, Table 2 compares the steady-state values of the contact force components for the rigid body model of the complete vehicle and for the model of the single flexible wheelset: a very good agreement of the two series of data is observed, leading to the conclusion that, at least for the considered running condition, the procedure introduce in Section 2.2 is able to correctly set-up the boundary conditions for the flexible wheelset model. Note that for the sake of brevity in Table 2 and below in this section, 'vertical', 'lateral' and 'longitudinal' force respectively mean the components of the contact force along the $\mathbf{Z}_T$, $\mathbf{Y}_T$ and $\mathbf{X}_T$ axes of the track-following reference, despite the $\mathbf{X}_T$- $\mathbf{Y}_T$- $\mathbf{Z}_T$ reference is rotated by the track cant angle.

5.1 Results for single harmonic rail corrugation

The first excitation case considered is rail corrugation having sinusoidal waveform with wavelength 60 mm, i.e. one tenth of the sleeper bay, and the corrugation amplitude is 2.42 μm that corresponds to the limit amplitude at 60 mm wavelength as defined by the ISO 3095 standard [18]. In Fig. 3 the vertical contact force generated by the wheelset travelling on the corrugated rail at 150 km/h is plotted as a function of time. The rail roughness profile is also reported in the figure using an appropriate scaling and offset to obtain a proper visualisation.

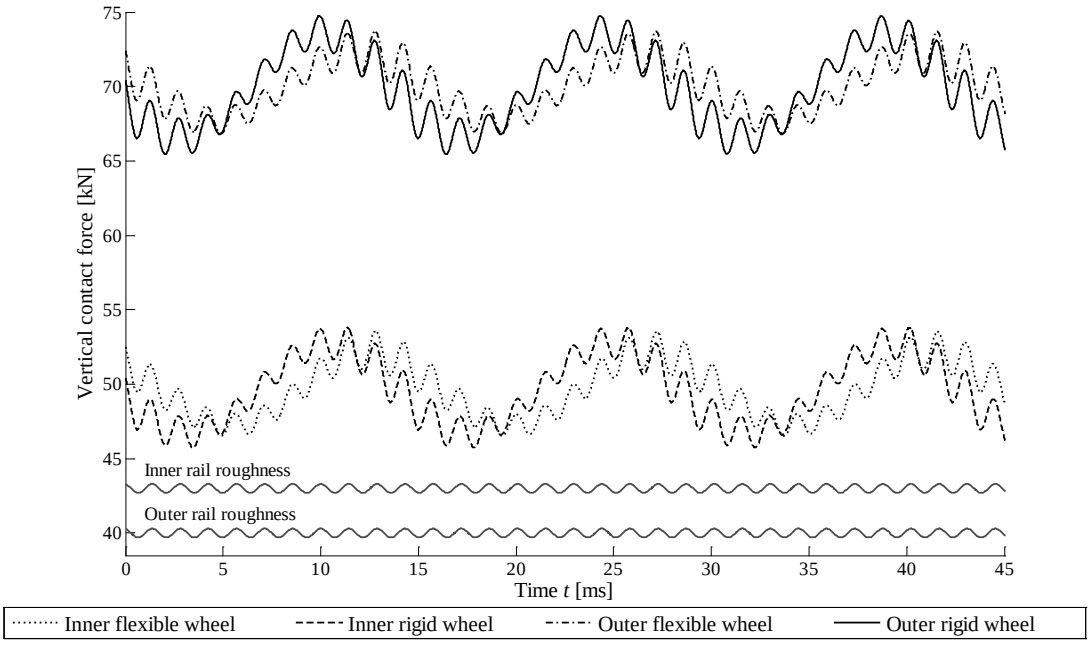

Figure 3: Vertical wheel-rail contact forces when the vehicle circulates at 150 km/h speed on a corrugated curved track (1000 m curve radius) with corrugation wavelength 60 mm. Corrugation amplitude corresponding to the ISO 3095 limit.

Two harmonic contents are observed in the vertical contact force, the largest one having the same wavelength as the rail corrugation and a second one with wavelength equal to the sleeper bay. This second harmonic component is due to the periodic variation of the rail stiffness seen by the wheelset as the consequence of the discrete rail support. The contact force is also highly affected by wheelset flexibility: considering a rigid wheelset leads to an over-estimation of the peak-to-peak dynamic force by approximately 15 per cent on the inner wheel and 40 per cent on the outer wheel. This is due to the fact that the mass participating in the high frequency vibration of the flexible wheelset is lower than the whole mass of the wheelset, mainly due to bending deformations occurring in the axle, a mechanism which is not captured by the rigid wheelset model.

Fig. 4 shows the lateral component of the contact force on the two wheels, for the same running condition considered above. The steady state values of the contact forces (see also Table 2) reflect the curving condition of the wheelset. Here, the leading wheelset in the front bogie of the vehicle is considered, for which a small negative angle of attack takes place on account of curve negotiation, causing a steady component of the transversal creep force which points towards the outside of the curve. This is balanced by the lateral component of the flange force on the outer wheel, leading to the typical condition of the two lateral forces pointing in opposite directions in a way that tends to widen the track gauge. Like for the vertical contact force component, the dynamic component of the lateral contact force shows two harmonic contents, one corresponding to the sleeper-passing frequency, the other corresponding to the wavelength of the harmonic corrugation introduced as the

source of excitation. Also in this case, simplifying the problem to the case of a rigid wheelset leads to an over-estimation of the dynamic contact force harmonics synchronous with the corrugation. The longitudinal contact force component caused by a single harmonic rail corrugation is not shown as the level of dynamic excitation for this case is very low.

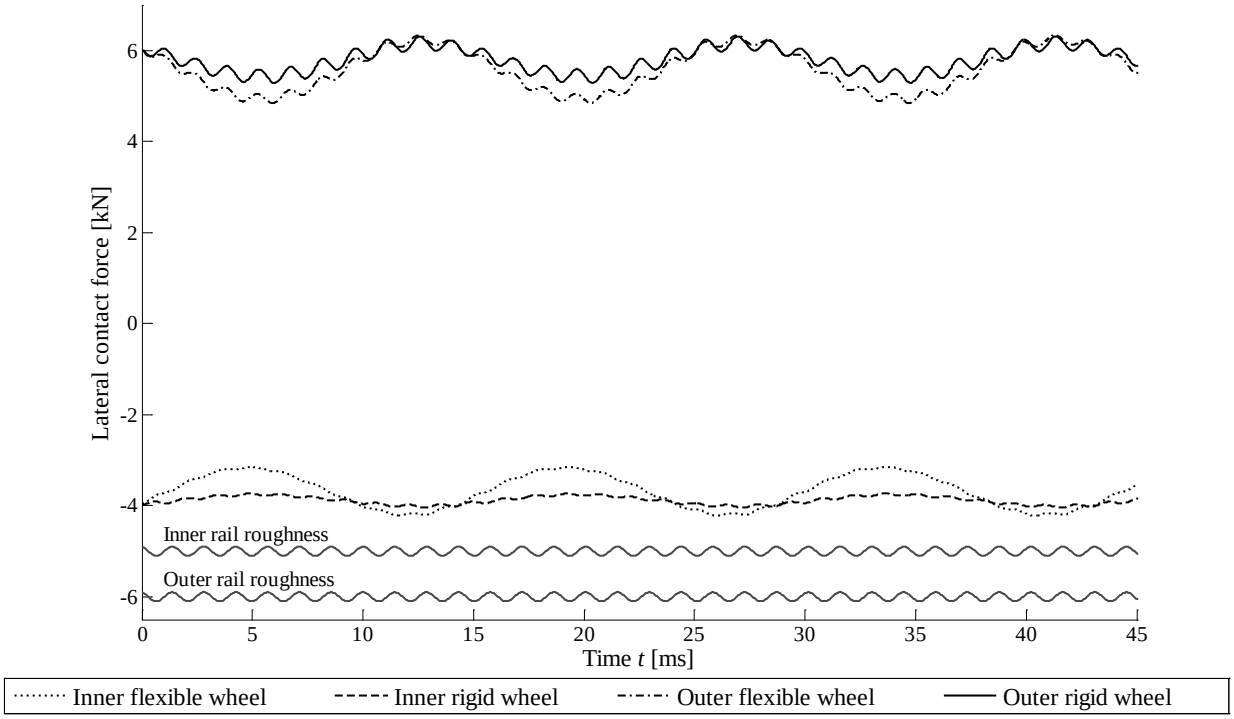

Figure 4: Lateral wheel-rail contact forces when the vehicle circulates at 150 km/h speed on a corrugated curved track (1000 m curve radius) with corrugation wavelength 60 mm. Corrugation amplitude corresponding to the ISO 3095 limit.

5.2 Results for random rail corrugation

Figs. 5, 6 and 7 show the time history of the vertical, lateral and longitudinal contact forces for excitation caused by randomly corrugated rails, assuming a corrugation spectrum corresponding to the ISO 3095 limit, which establishes a third-octave band spectrum of the rail roughness. The corrugated profiles of the rails are assumed as two independent stochastic processes, given the relatively short wavelengths involved. Hence, the irregularity of the *r*-th rail is generated according to:

$$z_r(x) = \sum_j A_j \cos\left(\frac{2\pi x}{\lambda_j} + \alpha_{jr}\right), \tag{42}$$

where A_j is the amplitude at the *j*-th wavelength λ_j of the ISO 3095, and α_{jr} is a random phase angle in rail *r*.

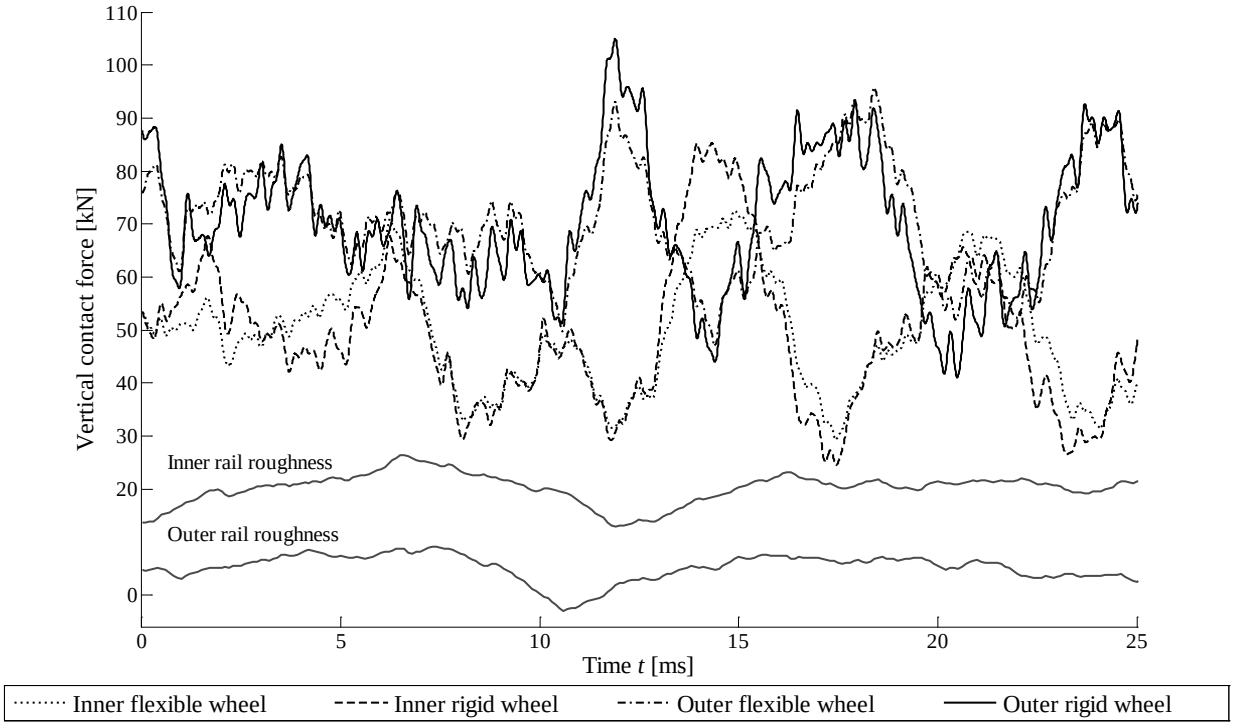

Figure 5: Vertical wheel-rail contact forces when the vehicle circulates at 150 km/h speed on a randomly corrugated curved track (1000 m curve radius). Amplitudes corresponding to the ISO 3095 limit.

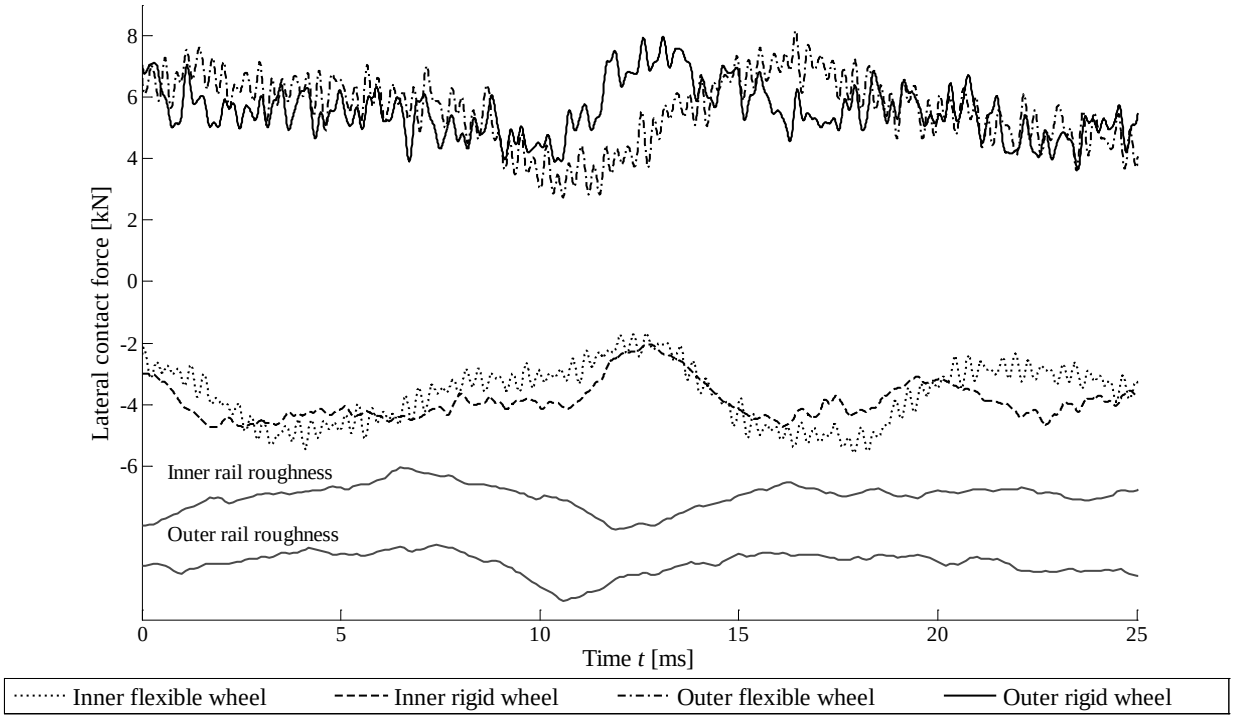

Figure 6: Lateral wheel-rail contact forces when the vehicle circulates at 150 km/h speed on a randomly corrugated curved track (1000 m curve radius). Amplitudes corresponding to the ISO 3095 limit.

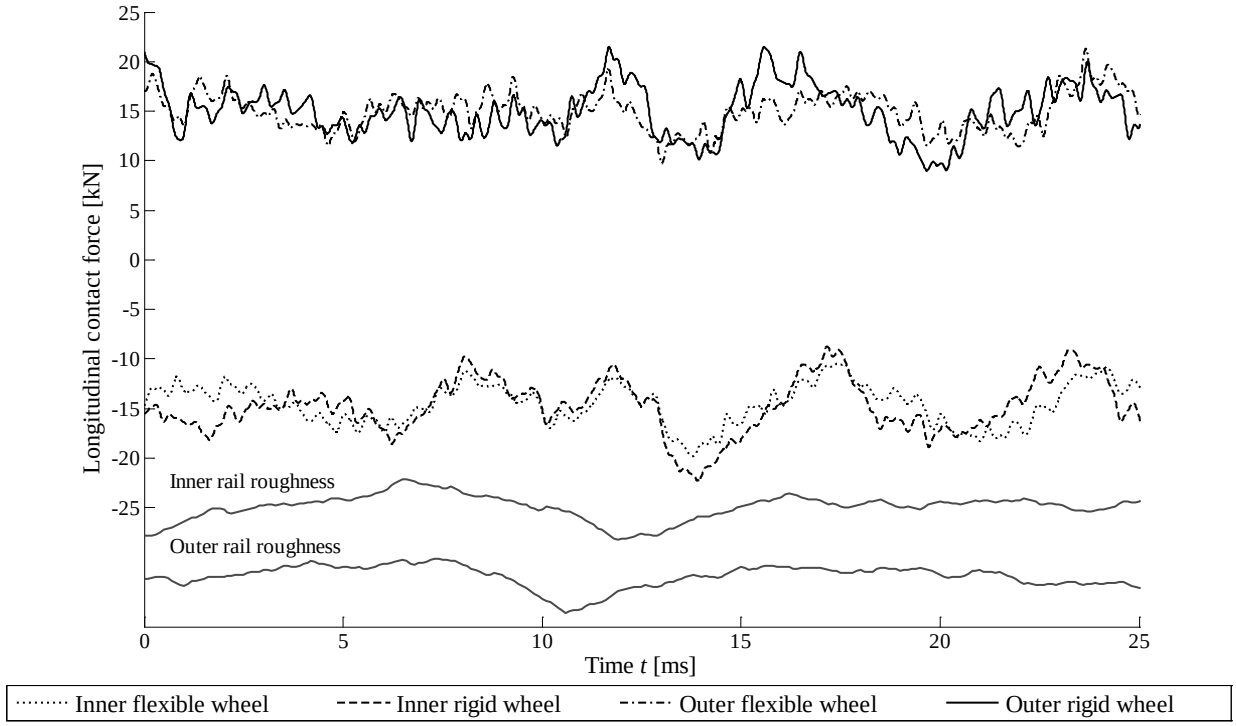

Figure 7: Longitudinal wheel-rail contact forces when the vehicle circulates at 150 km/h speed on a randomly corrugated curved track (1000 m curve radius). Amplitudes corresponding to the ISO 3095 limit.

The results obtained for a flexible and a rigid wheelset model are again compared. As expected, the dynamic fluctuations of all contact force components show a complex waveform, arising from the dynamic response of the wheelset-track system to broadband random excitation. As far as the vertical contact force component is concerned, this leads to a maximum dynamic force on the outer wheel which is 1.5 times the steady-state value in full curve, whereas on the inner wheel the minimum contact force is approximately 0.5 times the steady state value.

Compared to the results obtained using the flexible wheelset model, the use of a rigid wheelset model results in a significant over-estimation of the maximum force on the outer wheel and of the maximum wheel unloading on the inner wheel. However, for the lateral and longitudinal contact force components the situation is somewhat different, as the maximum amplitude of dynamic variations for the flexible and rigid wheelset model is comparable on both the outer and inner wheels, but with important differences in the waveform of the signals.

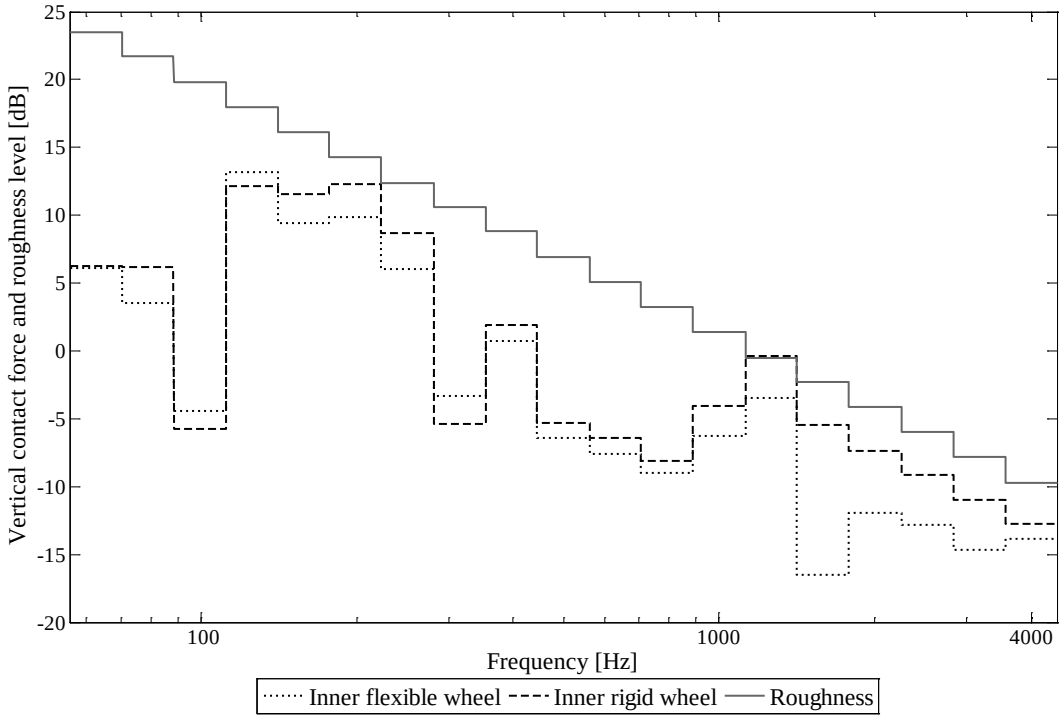

Figure 8: Frequency domain plot of the vertical wheel-rail contact forces in the inner wheel when the vehicle circulates at 150 km/h on a randomly corrugated curved track (1000 m curve radius), and the rail roughness spectrum of the ISO 3095 limit. Forces are referred to 1 kN; roughness is referred to 1 μm.

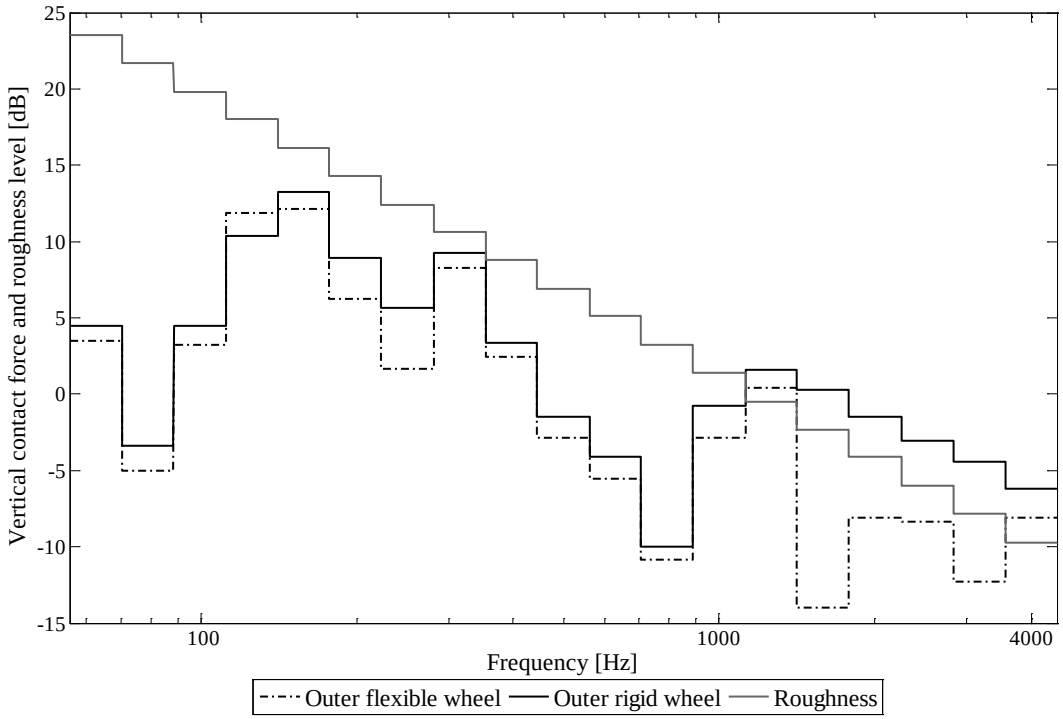

Figure 9: Frequency domain plot of the vertical wheel-rail contact forces in the outer wheel when the vehicle circulates at 150 km/h on a randomly corrugated curved track (1000 m curve radius), and the rail roughness spectrum of the ISO 3095 limit. Forces are referred to 1 kN; roughness is referred to 1 μm.

An alternative representation of the wheel-rail contact forces can be made in the frequency domain. Figs. 8 and 9 represent the third-octave band spectrum of the inner and outer wheel forces, respectively. These plots have been carried out for the rigid and the proposed models in dB (referred to 1 kN), and they also represent the rail roughness in the frequency domain (referred to 1 μm). There are peaks in the antiresonance of the track frequency (between the P2 and pinned-pinned frequencies, in the 100-300 Hz band), whereas the smaller responses are at the P2 (below 100 Hz) and pinned-pinned (below 1 kHz) frequencies. The main differences of the rigid and flexible models are above 1 kHz, where there exist many resonances of the wheelset.

5.3 Results for a wheel flat

Figs. 10, 11 and 12 show the time history of the vertical, lateral and longitudinal contact forces respectively caused by a wheelflat when the wheelset runs over a perfectly even track. In the simulations, a rounded geometry of the wheel flat [19] with size 50 mm was adopted. The same wheel flat is assumed to occur on both wheel profiles, with in-phase out-of-roundness profile.

It should be noted that, in principle, the presence of a wheel flat causes the wheelset to lose the polar symmetry so that the use of Eulerian coordinates, as introduced in Section 2, becomes unfeasible. However, due to the very small size of the wheel flat compared to the size of the wheels (the maximum deviation from circularity is approximately equal to 1/1000 of the wheel radius), the effect of wheel out-of-roundness on the elastic and inertial properties of the wheelset can be neglected, and only the geometric effect of the wheel flat needs to be considered, in the form of a periodic wheel-rail relative irregularity.

Results are presented for the same running condition in curved track considered in Section 5.1 and 5.2. The wheel flat is assumed to occur on the inner and outer wheel at the same time. Intense dynamic effects are observed, initially leading to the occurrence of full loss of contact at both wheels, then followed by a severe impact causing peaks in all force components, and finally by a transient vibration that generates further dynamic fluctuations in all contact force components.

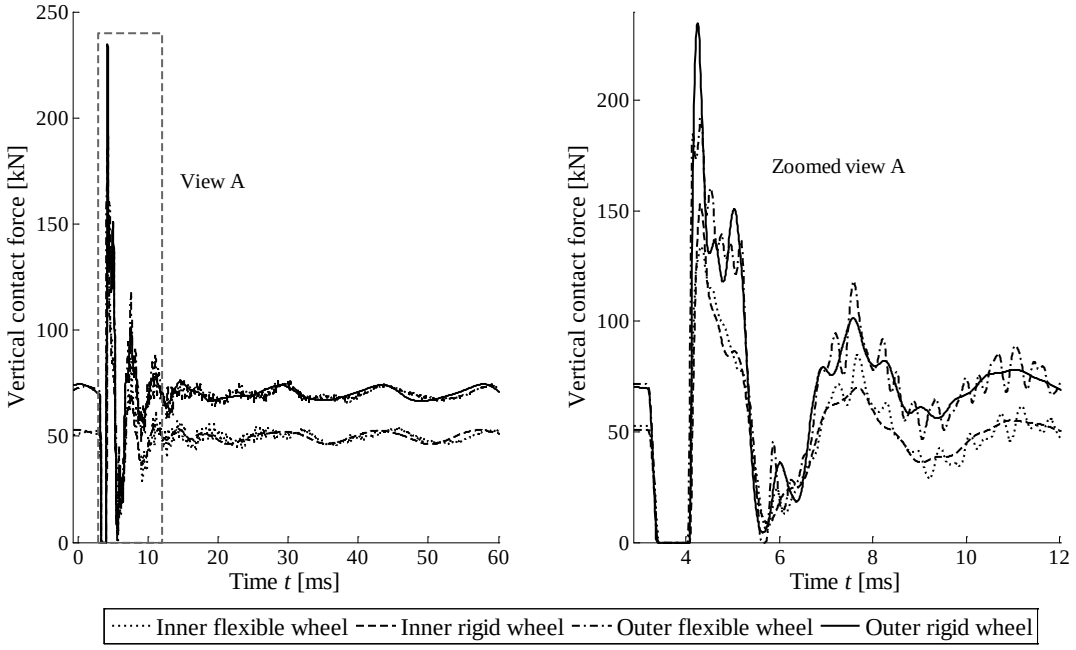

Figure 10: Vertical wheel-rail contact forces when the vehicle circulates at 150 km/h speed on a perfectly even curved track (1000 m curve radius) in presence of a 50 mm wheelflat.

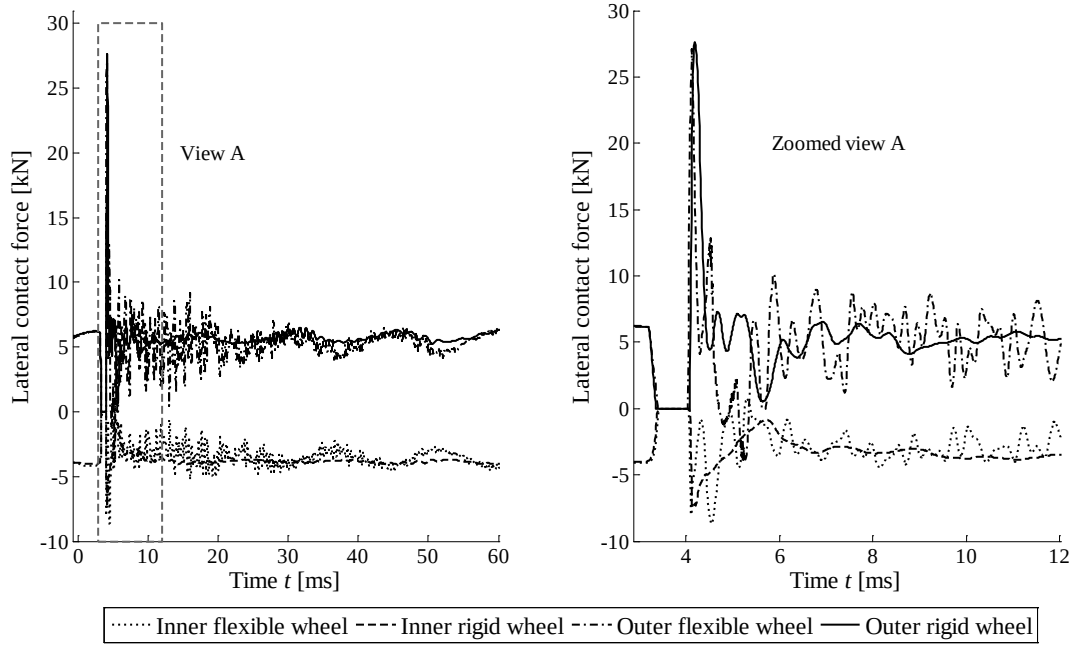

Figure 11: Lateral wheel-rail contact forces when the vehicle circulates at 150 km/h speed on a perfectly even curved track (1000 m curve radius) in presence of a 50 mm wheelflat.

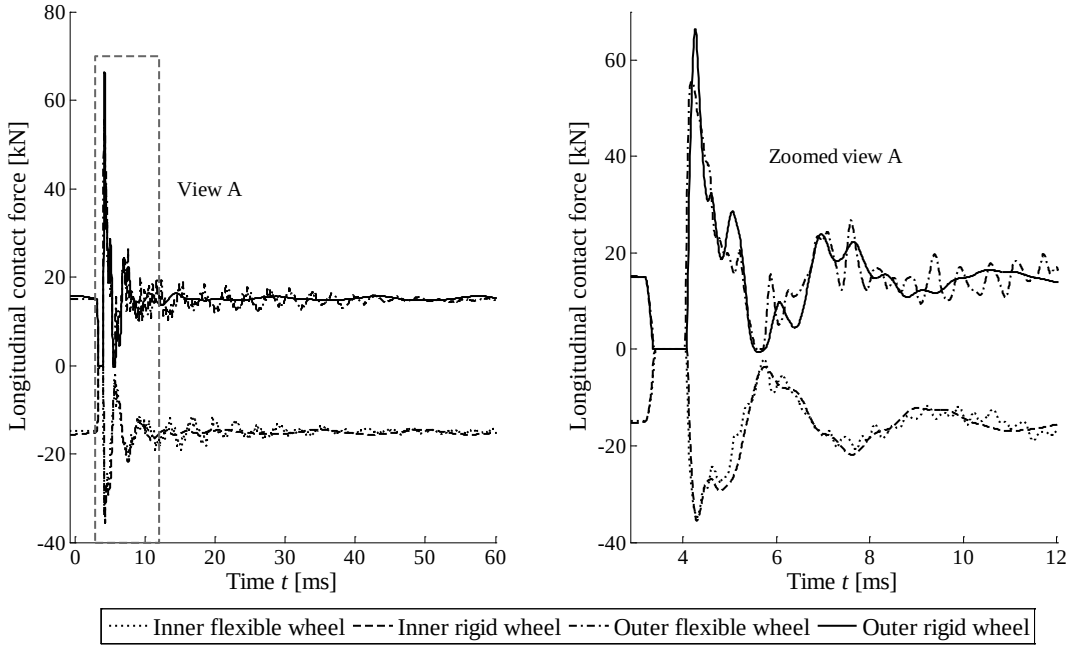

Figure 12: Longitudinal wheel-rail contact forces when the vehicle circulates at 150 km/h speed on a perfectly even curved track (1000 m curve radius) in presence of a 50 mm wheelflat.

As far as the vertical contact force component is concerned, the maximum overloading on the inner wheel is 306 per cent of the steady-state load, whereas on the outer wheel the maximum overloading reaches 335 per cent of the steady state load. For the lateral force component (Fig. 11), the peak load is much larger on the outer wheel than on the inner one, on account of the larger contact angle experienced by the outer wheel as a consequence of the lateral shift of the leading wheelset towards the outside of the curve: this is an effect that is not captured by models neglecting curving effects. Also for the longitudinal contact force component (Fig. 12) the peak value is larger on the outer wheel, on account of the larger normal contact force occurring on that wheel, which generates then a larger creep force for the same or similar creepage condition.

The differences between the results for the rigid and flexible wheelset model are small in terms of duration of the contact loss and of maximum overloading in lateral direction (the rigid wheelset model over-estimates the peak lateral load on the outer wheel by 2 per cent approximately with respect to the flexible wheelset model), but the transient following the impact is affected quite remarkably by wheelset flexibility, as demonstrated by the fluctuations of the contact force components following the impact. Furthermore, the maximum value of the vertical and longitudinal contact forces on the outer wheel is much larger when the rigid wheelset model is used, with an increase in the range of 22 and 20 per cent respectively.

In Fig. 13 results are presented for the same wheelset excitation considering the vehicle running at the same speed (150 km/h) in tangent track. Because dynamic effects in lateral and longitudinal direction are in this case relatively modest, only the vertical force component is shown. Furthermore, because of the symmetry in the running condition considered, the forces on the two wheels are the same and therefore results are shown for one single wheel. Apart from the difference in the steady state value of the contact forces, the waveform of the contact force time history in Fig. 13 looks similar to the result obtained for curve negotiation in Fig. 10. However, the peak force is approximately 180 kN, compared to 235 kN for the outer wheel in the curving condition, showing that wheelflat excitation in a curve may lead to considerable overloading of the wheelset and rails and can therefore be expected to cause accelerated damage and degradation of the contacting surfaces as well as increased noise and vibration.

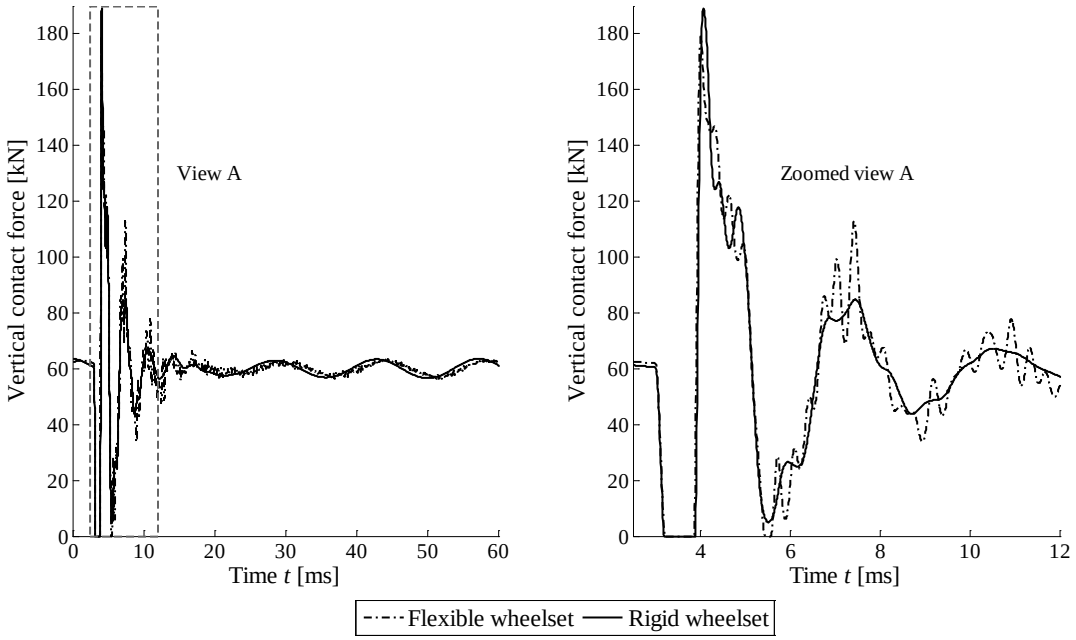

Figure 13: Vertical wheel-rail contact forces when the vehicle circulates at 150 km/h speed on a perfectly even tangent track in presence of a 50 mm wheelflat.

6. CONCLUSIONS

This paper has presented a model for a flexible wheelset running on a flexible curved track. By introducing a trajectory coordinates set describing the large motion of the wheelset along the curved track and assuming small relative movements of the wheelset with respect to the trajectory frame, the terms appearing in the wheelset equations of motion can be efficiently computed, keeping the

time required to carry the numerical simulation within acceptable limits. The flexible wheelset is coupled to a periodic curved track model by a non-linear description of wheel-rail contact forces.

Appropriate boundary conditions are prescribed at the wheelset axle-boxes in terms of vertical and lateral forces and longitudinal displacements above the primary suspension, to correctly reproduce the steady state contact forces and creepages as obtained from a simulation of the low frequency running dynamics of the complete vehicle along the curve considered. The results reported in Table 2 show that this method succeeds in establishing the appropriate steady state contact condition on both wheels, for the exemplary curving condition considered in this paper, which consists of the wheelset running at 150 km/h along a 1000 m radius curve with a track cant of 150 mm.

Results are presented for three types of excitation: single harmonic rail corrugation, randomly corrugated track and excitation arising from a wheel flat when the wheelset runs over a perfectly even track. To point out the implications of modelling wheelset flexibility, results are also presented for the case of a rigid wheelset.

In all three excitation cases considered, the rigid wheelset model leads to an over-estimation of the maximum contact forces, compared to the flexible wheelset model. However, in case of wheel flat excitation, small difference of the results obtained for the rigid and flexible wheelset model is observed for the lateral component of the contact force.

Finally, for the case of wheel flat excitation results obtained for the wheelset running in curve were compared to the case of the wheelset running at the same speed in tangent track: this comparison shows that the peak load in the vertical force component is approximately 30 per cent larger when the wheelset runs in curve compared to the tangent track running case, leading to the conclusion that wheelflat excitation in a curve may lead to considerable overloading of the wheelset and rails and can therefore be expected to cause accelerated damage and degradation of the contacting surfaces as well as increased noise and vibration.

ACKNOWLEDGEMENTS

The authors acknowledge the financial contribution of the Spanish Ministry of Economy and Competitiveness through the projects TRA2013-45596-C2-1-R.

REFERENCES

[1] D. J. Thompson, Railway Noise and Vibration: Mechanisms, Modelling and Means of Control, Elsevier, Oxford, UK, 2009.

[2] J. C. O. Nielsen, R. Lundén, A. Johansson, T. Vernersson, Train-track Interaction and Mechanisms of Irregular Wear on Wheel and Rail Surfaces, Vehicle System Dynamics 40 (1-3) (2003) 3-54.

[3] A. Ekberg, Fatigue of railway wheels, In: The Wheel/Rail Interface Handbook Woodhead Publishing in Mechanical Engineering, (2009) 211-244.

[4] S.L. Grassie, R.W. Gregory, D. Harrison, K. L. Johnson, Dynamic response of railway track to high frequency vertical excitation, Journal of Mechanical Engineering Science 24 (1982) 77-90

[5] G. Diana, F. Cheli, S. Bruni, A. Collina, Experimental and numerical investigation on subway short pitch corrugation, Vehicle System Dynamics 29 (Suppl.) (1998) S234-S245.

[6] A. Johansson, Out-of-Round Railway Wheels – Causes and Consequences: An Investigation Including Field Tests, Out-of-Roundness Measurements and Numerical Simulations, Doctoral dissertation, Chalmers University, September 2005.

[7] K. Popp, I. Kaiser, Interaction of elastic wheelsets and elastic rails: modelling and simulation, Vehicle System Dynamics 44 (Suppl.) (2006) S932-S939.

[8] D. J. Thompson, C. J. C. Jones, A Review of the Modelling of Wheel/Rail Noise Generation, Journal of Sound and Vibration 231 (3) (2000) 519-536.

[9] I. Kaiser, Refining the modelling of vehicle-track interaction, Vehicle System Dynamics 50 (Suppl.) (2012) S229-S243.

[10] L. Baeza, J. Fayos, A. Roda, R. Insa, High frequency railway vehicle-track dynamics through flexible rotating wheelsets, Vehicle System Dynamics 46 (7) (2008) 647-662.

[11] P. T. Torstensson, J. C. O. Nielsen, L. Baeza, Dynamic train-track interaction at high vehicle speeds-Modelling of wheelset dynamics and wheel rotation, Journal of Sound and Vibration 330 (2011) 5309-5321.

[12] S. Bruni, A. Collina, G. Diana, P. Vanolo, Lateral dynamics of a railway vehicle in tangent track and curve: tests and simulation, Vehicle System Dynamics 33 (Suppl.) (2000) S464-S477.

[13] L. Baeza, H. Ouyang, A railway track dynamics model based on modal substructuring and a cyclic boundary condition, Journal of Sound and Vibration 330 (2011) 75-86.

[14] J. Piotrowski, H. Chollet, Wheel-rail contact models for vehicle system dynamics including multi-point contact, Vehicle System Dynamics 43 (6) (2005) 455-483.

[15] F. Braghin, S. Bruni, G. Diana, Experimental and numerical investigation on the derailment of a railway wheelset with solid axle, Vehicle System Dynamics 44 (4) (2006) 305-325.

[16] Z. Y. Shen, J. K. Hedrick, J. A.Elkins, A comparison of alternative creep force models for rail vehicle dynamic analysis, Vehicle System Dynamics 12 (Suppl.) (1983) S79-S82.

[17] L. Mazzola, Y. Bezin, S. Bruni, Vehicle-Track interaction: MB simulation for track loading limits and damage identification ECCOMAS Thematic Conference Multibody Dynamics 2011, July 4-7 2011, Brussels, Belgium.

[18] ISO 3095:2005. Railway applications. Acoustics. Measurement of noise emitted by railbound vehicles, CEN, Brussels, August 2005.

[19] L. Baeza, A. Roda, J. Carballeira, E. Giner, Railway Train-Track Dynamics for Wheelflats with Improved Contact Models, Nonlinear Dynamics 45 (2006) 385-397.